

An ellipsoid convex enhancement filter for detection of asymptomatic intracranial aneurysm candidates in CAD frameworks

靳, 泽

<https://doi.org/10.15017/1785357>

出版情報：九州大学, 2016, 博士（保健学）, 課程博士
バージョン：
権利関係：全文ファイル公表済



Doctoral Thesis

An ellipsoid convex enhancement filter for detection of
asymptomatic intracranial aneurysm candidates
in CAD frameworks

Division of Medical Quantum Science, Department of Health Sciences,
Graduate School of Medical Sciences, Kyushu University

Student ID: 3MD13515Y

Ze Jin

April 20, 2016

An ellipsoid convex enhancement filter for detection of asymptomatic intracranial aneurysm
candidates in CAD frameworks

Department of Health Sciences

3MD13515Y

Ze Jin

Purpose: Various kinds of enhancement filters have been developed in computer-aided diagnostic (CAD) frameworks for asymptomatic intracranial aneurysms in magnetic resonance angiography (MRA). However, many bending or branching portions on vessels are also enhanced by the conventional filters as false positives in 3.0 T MRA, which can visualize smaller vessels compared with 1.5 T MRA. To overcome this problem, this study focused on developing an ellipsoid convex enhancement (ECE) filter, which can selectively enhance aneurysms while reducing false positive contrasts on bending or branching portions on vessels, for detection of asymptomatic intracranial aneurysm candidates in CAD frameworks.

Materials and Methods: The ECE filter was mathematically designed to enhance various convex regions in the intensity space such as convex aneurysms, in which the ratio of the shortest and longest diameters for aneurysms corresponds to the ratio of reciprocals of the square roots of the first and third eigenvalues of a Hessian matrix. The proposed ECE filter was evaluated by measuring an average contrast for false positive models and free-response receiver operating characteristic curves between two simple CAD frameworks using the ECE and conventional filters based on a leave-one-out-by-patient test. MRA images for thirty patients (Male: 10, Female: 20; age: 48 to 86 years, mean: 69.2) with 31 unruptured aneurysms (longest diameter: 2.0 to 5.5 mm, mean: 3.7 mm) were selected for this study.

Results: The average contrast for false positive models was reduced by 51.4% using the ECE filter, compared with the conventional filter for the convex regions with ratios of the shortest and longest diameter less than 0.4. The number of false positives per case was decreased from 41.1 to 22.8 on average at a

sensitivity of 87% by using the ECE filter.

Conclusions: The ECE filter would be useful for boosting the performance of the CAD framework of asymptomatic intracranial aneurysms by providing higher contrast aneurysms and lower contrast false positives such as bending or branching portions on vessels.

Keywords: computer-aided diagnosis (CAD), unruptured intracranial aneurysm, magnetic resonance angiography (MRA), ellipsoid convex enhancement (ECE) filter

Contents

Chapter 1 Introduction	2
1.1. Background	2
<i>1.1.1. Intracranial aneurysm</i>	<i>2</i>
<i>1.1.2. Magnetic resonance angiography for detection of intracranial aneurysm</i>	<i>3</i>
<i>1.1.3. Computer-aided diagnosis system</i>	<i>4</i>
<i>1.1.4. Conventional studies of CAD system for detection of intracranial aneurysm</i>	<i>5</i>
1.2. Purpose	8
Chapter 2 Development of a CAD framework.....	9
2.1. Clinical cases.....	9
2.2. Methodology	11
<i>2.2.1. Extraction of a VOI in an MRA image</i>	<i>12</i>
<i>2.2.2. A 3D blob enhancement filter</i>	<i>14</i>
<i>2.2.3. Multiple-gray-level thresholding and initial candidates selection.....</i>	<i>14</i>
<i>2.2.4. Segmentation of initial aneurysm regions using a region growing method.....</i>	<i>15</i>
<i>2.2.5. Image features and FP removal</i>	<i>16</i>
2.3. Evaluation method	19
2.4. Problems and solutions	21
Chapter 3 Theory of an ellipsoid convex enhancement filter	24
3.1. Mathematical design of ECE filter.....	24

3.2. Evaluation of ECE filter	28
3.2.1 <i>Gaussian ellipsoid models of various convex regions for evaluation</i>	28
3.2.2 <i>A conventional method for enhancement of convex regions</i>	30
3.3. Results	31
3.4. Discussion	37
Chapter 4 Conclusions	39
Acknowledgement.....	40
References	41
Achievements	46

Abbreviations and keywords

Abbreviation	Full spelling	Explanation
CAD	Computer-Aided Diagnosis	In radiology, computer-aided diagnosis, also called computer-aided detection, are procedures that assist doctors or radiologists in the interpretation of medical images.
ECE	Ellipsoid Convex Enhancement	The ECE filter was mathematically designed to enhance various convex regions in the intensity space such as convex aneurysms, in which the ratio of the shortest and longest diameters for aneurysms corresponds to the ratio of reciprocals of the square roots of the first and third eigenvalues of a Hessian matrix.
FP	False Positive	A FP is an error in data reporting in which a test result improperly indicates presence of a condition when in reality it is not.
MRA	Magnetic Resonance Angiography	MRA is a group of techniques based on MRI to image blood vessels, which is used to generate images of vessels in order to evaluate them for aneurysms, stenosis (abnormal narrowing), occlusions (blockage of a blood vessel), or other abnormalities..
MIP	Maximum Intensity Projection	MIP is a volume rendering method for 3D data that projects in the visualization plane the voxels with maximum intensity that fall in the way of parallel rays traced from the viewpoint to the plane of projection.
SVM	Support Vector Machine	In machine learning, SVMs are supervised learning models with associated learning algorithms that analyze data used for classification and regression analysis.
UIA	Unruptured Intracranial Aneurysm	UIA is a cerebrovascular disorder in the brain, causing a localized dilation or ballooning arising from a weakened area in the wall of a blood vessel
VOI / ROI	Volume Of Interest / Region Of Interest	A VOI/ROI is a selected subset of samples within a dataset identified for a particular purpose.

Chapter 1 Introduction

1.1. Background

1.1.1. Intracranial aneurysm

An intracranial aneurysm (also called a cerebral aneurysm) is a cerebrovascular disorder in the brain, causing a localized dilation or ballooning arising from a weakened area in the wall of a blood vessel [1]. Basically, there are two types of aneurysms, i.e. saccular aneurysm and fusiform aneurysm, which are categorized by their geometries. Figure 1.1 shows illustrations for two types of aneurysms [2]. Prospective autopsy and angiographic studies indicated that the prevalence of intracranial aneurysms was estimated to be between 3.6% and 6.0% of the general population [3]. If the brain aneurysm expands and the blood vessel wall becomes too thin, the aneurysm will rupture and bleed into the space around the brain, which is called subarachnoid hemorrhages (SAH). The SAH is a serious disorder that may cause a hemorrhagic stroke, 60% of patients could die immediately after rupture [4]. Therefore, asymptomatic unruptured intracranial aneurysms (UIA) should be detected as early as possible prior to their rupture.

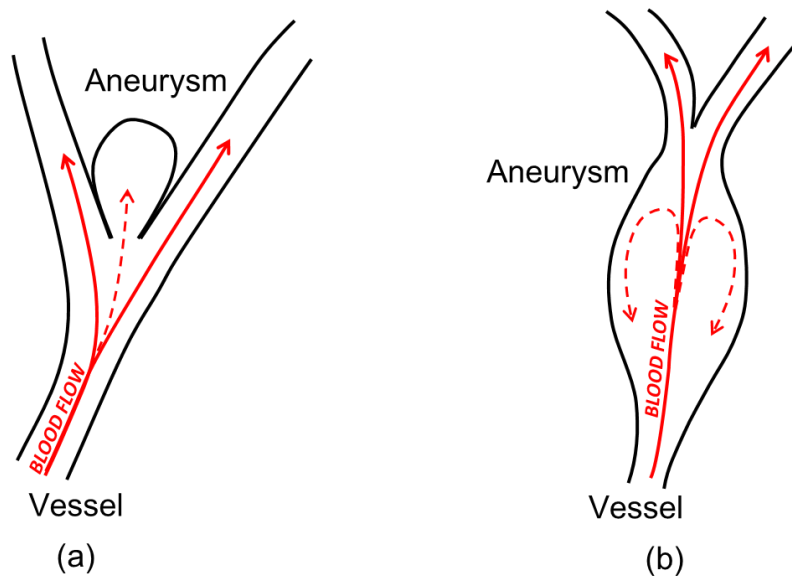


FIG. 1.1. Illustrations of two typical type aneurysms: (a) a saccular aneurysm and (b) a fusiform aneurysm.

Red arrows show the blood flow.

1.1.2. Magnetic resonance angiography for detection of intracranial aneurysm

Most unruptured intracranial aneurysms are detected during routine imaging of the brain [5]. Therefore, for early detections of asymptomatic intracranial aneurysms, the standard modality for the first screening is magnetic resonance angiography (MRA). MRA is used to generate images of vessels in order to evaluate them for aneurysms, stenosis (abnormal narrowing), occlusions (blockage of a blood vessel), or other abnormalities. It is widely used for the advantage of less toxic and non-invasive without using contrast agents, compared with computed tomography (CT) angiography or catheter angiography [6, 7]. Figure 1.2 shows three MIP images of aneurysms cases. The aneurysms are indicated by yellow arrows.

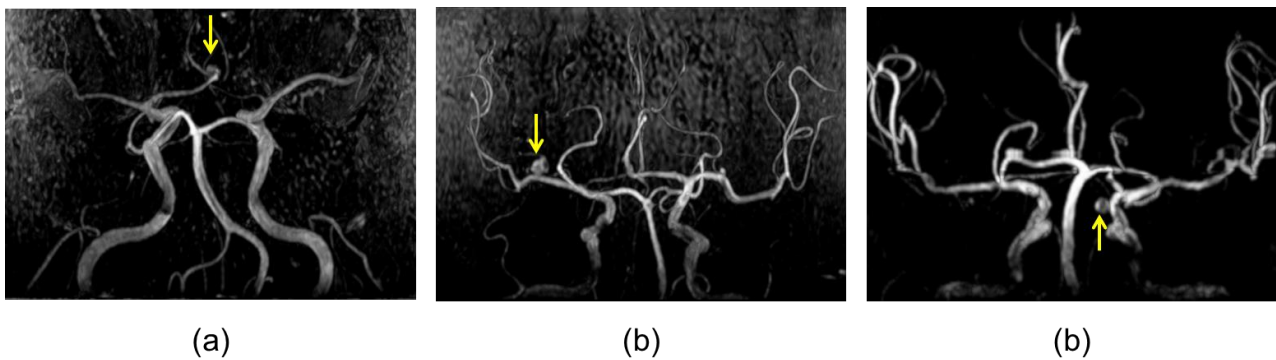


FIG. 1.2. Three MIP images of aneurysms cases. The aneurysms are indicated by yellow arrows.

In recent years, a high level of interest in the prevention of stroke and dementia has led to a health check system for intracranial and cerebrovascular diseases, which is now widely performed in Japan by the name of "The Brain Dock". The items of checking include images of MRI and MRA making the diagnosis possible for asymptomatic UIA or asymptomatic intracranial infarctions. In 1995 a national wide survey revealed that the brain dock is available in approximately 500 institutes in Japan and, it is detecting UIA in 2.7% and asymptomatic intracranial infarctions in 20.4% of the applicants. By using more sophisticated methods of detection, it is possible to detect UIA in more than 5% of the applicants if they are older than 50 years of age [8].

Despite these advantages of the brain dock, it is hard and time consuming for radiologists to detect aneurysms because of overlapping structures in the maximum intensity projection (MIP) images and/or unusual locations, especially for aneurysms smaller than 7 mm [9,10]. During the popularization of the brain dock, an explosive growth of interpretation of medical images made it is substantially difficult for the unexperienced radiologists. Therefore, to research and develop computer-aided diagnosis (CAD) systems, which could help radiologists in detection of aneurysms is an issue in recent years, especially for the small aneurysms that might be missed by human eyes.

1.1.3. Computer-aided diagnosis system

In radiology, computer-aided diagnosis, also called computer-aided detection, are procedures that assist doctors or radiologists in the interpretation of medical images. CAD systems can help doctor or radiologists in proving lesion candidates, highlight conspicuous sections or segmentation of organ regions, etc. [11]. CAD systems utilize pattern recognition technologies, including computer vision with image processing and machine learning techniques. The typical procedures of CAD systems are described in Fig. 1.3.

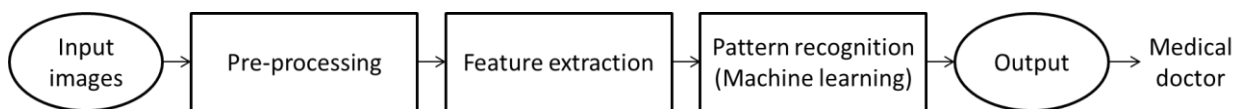


FIG. 1.3. The typical procedures of CAD systems.

In the case of medical imaging, especially the MR imaging, because the image quality is often changing for each patient or per imaging sequence, pre-processing is a very important process. Pre-processing is a necessary process in order to facilitate the feature extraction. The following action will be considered as a pre-treatment: reduction of artifacts, noise reduction processing (smoothing), edge enhancement (sharpening), normalization of pixel values, geometrical transformation, and extraction of region of interest, etc.

Feature extraction process is the most important process, for which a number of techniques have been developed. Generally, it is constituted by enhancement of specific pattern, detection of initial candidate regions, segmentation of candidates, and calculation of features. For example, aneurysms often appear to be a local intensity convex blob region in MRA images. The certain gradient information could be one of the features of aneurysms for recognition of aneurysm-liked structures. The following action will be considered as a feature extraction: detection of edge, corner, blob, and ridge, scale-invariant feature transform, calculation of curvature on edges, and extraction of intensity based features such as average intensity and standard deviation, etc.

Pattern recognition algorithms generally aim to provide a reasonable answer for all possible inputs and to perform "most likely" matching of the inputs features, taking into account their statistical variation. The pattern recognition is often done by machine learning methods, such as decision tree learning, support vector machine (SVM), artificial neural networks (ANN), and deep learning, etc.

The computer output could be used as a "second opinion" in assisting radiologist in image interpretations. Until now, CAD systems were developed and applied in the diagnosis of pathological brain detection [12-15], breast cancer [16-18], lung cancer [19], colon cancer [20, 21], prostate cancer, bone metastases, coronary artery disease [22-24], congenital heart defect, and Alzheimer's disease [25-27], etc. It is likely that CAD will become a standard tool for diagnosis in daily clinical work.

1.1.4. Conventional studies of CAD system for detection of intracranial aneurysm

For assisting radiologists in detection of intracranial aneurysms with the MRA, a number of automated identification systems have been developed [28-38]. Hirai *et al* [30] reported that the area under the receiver operating characteristic curve was increased significantly from 0.931 to 0.983 when a computer-aided diagnosis (CAD) system was used by radiologists. A recent study proposed by Šteřán-Buksakowska *et al*

[36] also showed a statistically significant improvement by using a CAD system for detection of intracranial digital subtraction angiography (DSA)-confirmed aneurysms less than 6 mm. Furthermore, Kakeda *et al* [32] proved that the use of a CAD system can shorten the reading time while improving diagnostic performance for less experienced radiologists.

In conventional studies of CAD systems for the detection of intracranial aneurysms, a strategy of enhancing aneurysms by using a sphere-enhancement filter or blob-enhancement filter was widely used for detection of initial candidates. The basic idea was to evaluate the local shapes by computing the Hessian matrix of Gaussian scaled intensity space. Sato *et al* [39] described an approach to tissue classification using three-dimensional (3D) derivative features in the volume for dot, line, and plane shapes, which can simultaneously enhance objects of specific shapes and suppress objects of other shapes. They designed 3D filters based on the gradient vector and Hessian matrix with multi-scales of the volume intensity function combined with isotropic Gaussian blurring to enhance blob, line and sheet structures, and used the filter outputs as multi-channel information for tissue classification. Frangi *et al* proposed a multiscale vessel enhancement filter, which can evaluate the vesselness according to all eigenvalues of the Hessian matrix. Their dissimilarity measure takes into account two geometric ratios based on the second order ellipsoid. One ratio accounts for the deviation from a blob-like structure. The other ratio refers to the largest area cross section of the ellipsoid [40]. Arimura *et al* [28] proposed a CAD scheme for detection of intracranial aneurysms in MRA with a dot-enhancement filter. Morphological and gray-level features were computed and a linear discriminant analysis was used to minimize the number of false positives. Similar kinds of filters were shown in other studies combined with other methods to improve the performance of CAD systems [31, 34, 37]. In the study by Yang *et al* [34], the output of the sphere-enhancement filter was analyzed for initial candidate selection, and a difference image was calculated by obtaining short branches from the skeletonized vasculature. In a recent study, Hentschke *et al* [37] proposed a detection method with

a blob-enhancement filter combined with a rule-based system and a non-linear classification, achieved 95% sensitivity at an average false positive rate per data set of 11.3.

Table 1.1 Comparison of conventional methods with different methods

Institute (year)	Method	Number of aneurysms	Imaging modality	Sensitivity	Number of FPs per case
Arimura <i>et al</i> (2004)	Hessian filter	36	MRA 1.5T	100%	2.4
Kobashi <i>et al</i> (2006)	Geometrical segmentation	19	MRA 1.5T	100%	6.4

Table 1.1 shows the comparison of conventional methods with different methods. The Hessian filter is superior, because less number of false positives.

Table 1.2 CAD studies based on Hessian filters

Institute (year)	Method	Number of aneurysms	Imaging modality	Sensitivity	Number of FPs per case
Yang <i>et al</i> (2011)	Hessian filter	147 (55 < 5 mm)	MRA (1.5T, 3T)	93%	6.5
Hentschke <i>et al</i> (2014)	Hessian filter	112 (all < 7 mm)	MRA (1.5T, 3T)	95%	11.3

The Hessian filter method was applied to large number of cases and MRA images with different magnetic field strength. Therefore, the purpose of our study is to develop a CAD framework based on the Hessian based enhancement filter.

1.2. Purpose

This study focused on developing an ellipsoid convex enhancement (ECE) filter, which can selectively enhance aneurysms while reducing contrasts of false positive structures, for detection of asymptomatic intracranial aneurysm candidates in CAD frameworks. In this paper, the background leading up to the purpose of the study is introduced in Chapter 1. In Chapter 2, development of a CAD framework is introduced. Chapter 3 is the depiction of the theory of an ellipsoid convex enhancement (ECE) filter. Finally, Chapter 4 is a summary of this thesis.

Chapter 2 Development of a CAD framework

This chapter includes the contents of the Ph.D. thesis “*An Ellipsoid Convex Enhancement Filter for Detection of Asymptomatic Intracranial Aneurysm Candidates in CAD Frameworks*”.

2.1. Clinical cases

This study was performed with approval by the Institutional Review Board of the Kyushu University Hospital and University of Occupational and Environmental Health. Thirty patients with 31 unruptured aneurysms (Male: 10, Female: 20; age: 48 to 86 years, mean: 69.2) who received MRA diagnosis during 2006-2007 or 2010-2014, were selected for this study. All aneurysms were confirmed by two experienced neuroradiologists (S.K. and Y.K.), by using computed tomographic angiography or DSA according to the guideline from the Japan Stroke Society [48]. MRA images of the patients were acquired on a 3.0 T MR imaging scanner (Signa Excite; General Electric, Milwaukee, WI, USA). The 3D MRA images included 112 to 172 slices per case with a slice thickness of 1 to 1.2 mm and a slices distance of 0.5 to 0.7 mm. The dimension of each axial image was 512×512 pixels with a pixel size of 0.3516 mm. Original 3D MRA images were converted to isotropic volume data with matrix sizes of $512 \times 512 \times (224-258)$ and an isotropic voxel size of 0.3516 mm by using a cubic interpolation method.

This study focused on detecting the aneurysms smaller than 7 mm, for the large aneurysms could be easily found by radiologists [9]. The sizes of aneurysms were manually measured in terms of a longest diameter, a shortest diameter which is perpendicular to the longest diameter and a middle diameter perpendicular to the longest and shortest diameters. The measurements were performed twice by each of the two observers, who were the first author (Z.J.) and a medical physicist (H.A.). Figure 2.1 shows the measurement of longest (light red dotted line), shortest (light blue solid line), and middle (yellow dashed line) diameters of an aneurysm in three planes, which are orthogonal to each other in MRA

images by using a multiplanar reconstruction software (Osirix; Newton Graphics, Inc.). Figure 2.2 shows the relationship between the longest diameter and the ratio of the shortest diameter to the longest diameter for 31 aneurysms. The longest diameters of 31 aneurysms ranged from 2.0 to 5.5 mm, with a mean length of 3.7 mm. The standard error of the mean for the measured diameters was 0.14 mm. The ratio of the shortest diameter to the longest diameter ranges from 0.45 to 0.90, with a mean value of 0.72.

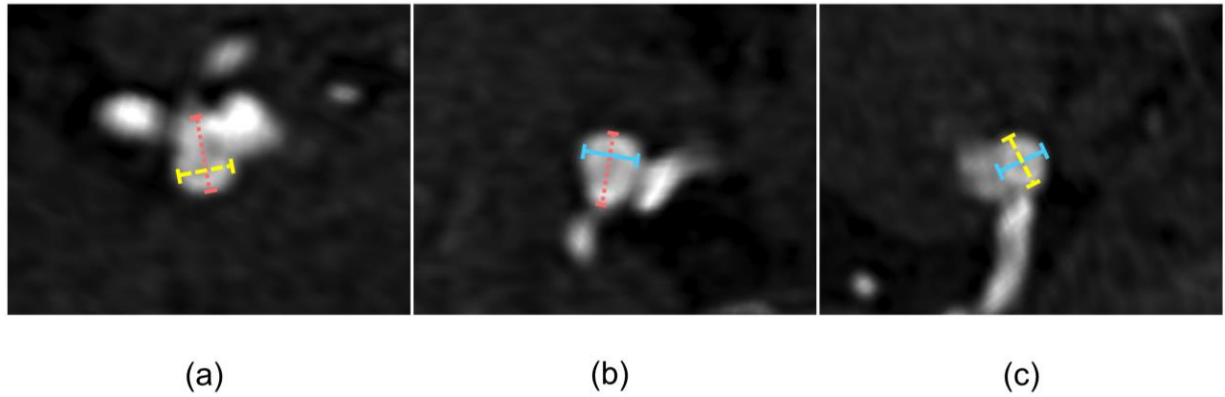


FIG. 2.1. Illustrations of measurement of longest (light red dotted line), shortest (light blue solid line), and middle (yellow dashed line) diameters of an aneurysm in three planes, which are orthogonal to each other in MRA images by using a multiplanar reconstruction software

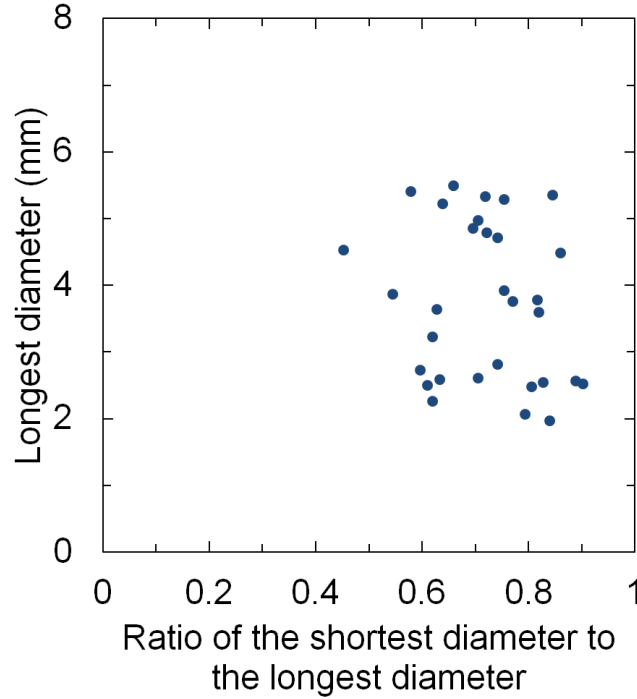


FIG. 2.2. Relationship between the longest diameter and the ratio of the shortest diameter to the longest diameter of 31 aneurysms.

2.2. Methodology

Figure 2.3 shows the overall scheme of the CAD framework of aneurysm candidates. First, the volumes of interest (VOI) for searching for the aneurysm candidates was determined based on vessel images extracted from the 3D MRA images using a region growing technique, because most aneurysms appear on specific vessels and their surroundings. Second, aneurysms were enhanced by using a blob structure (BSE) enhancement filter. Initial candidate points were selected after applying a multiple-gray-level thresholding method to the enhanced images. Initial aneurysm regions were segmented by a region growing method with monitoring some image features, which started from the initial candidate points. Third, a number of false positives were removed based on the rules which were made by investigation of image features associated with morphology and gray levels.

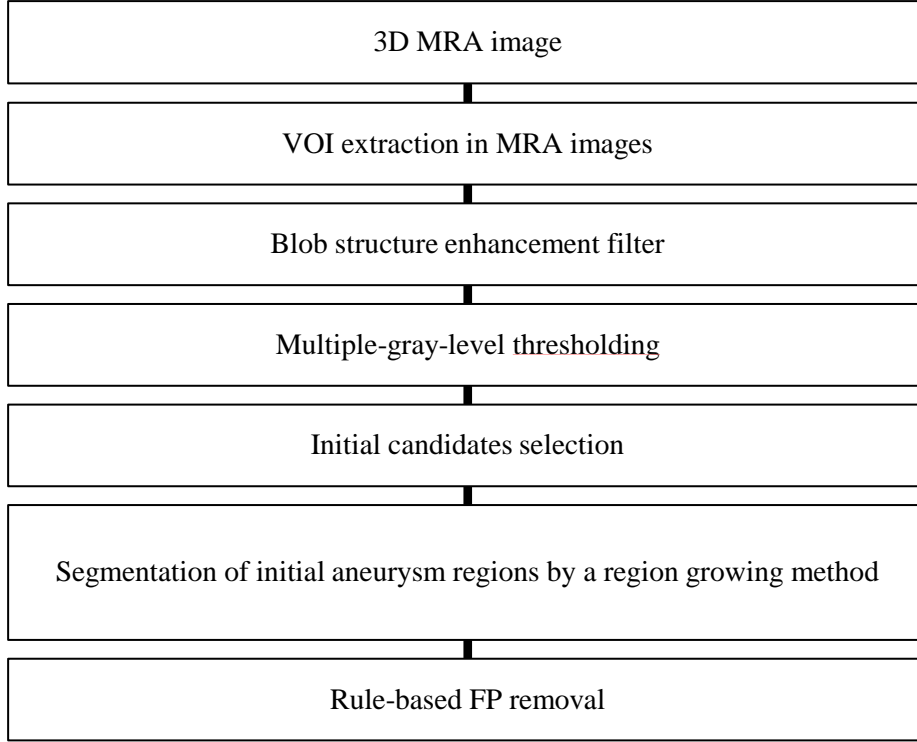
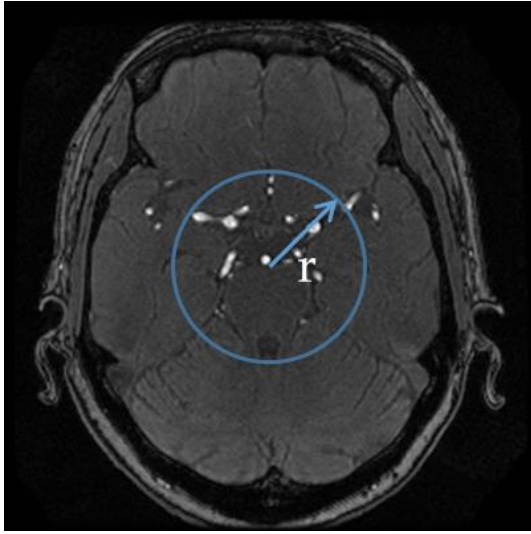


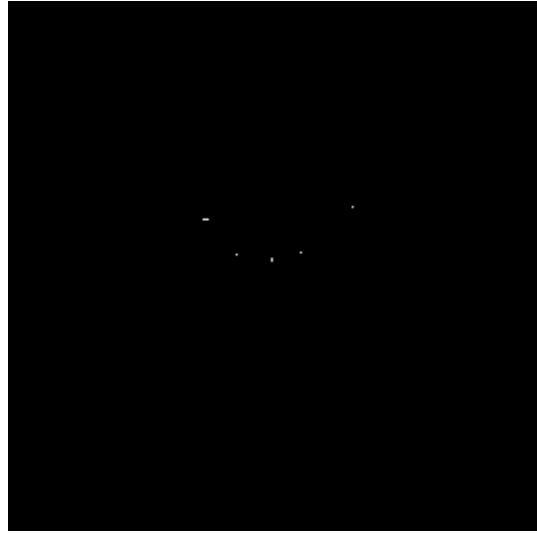
FIG. 2.3. The overall scheme of a CAD framework of aneurysm candidates.

2.2.1. Extraction of a VOI in an MRA image

The VOI for finding aneurysm candidates was determined based on the regions of the main vessels that extracted from the 3D MRA images by using a region growing technique [49]. Figure 2.4 shows illustrations of extraction of a VOI in an MRA image. First, the maximum voxel value was selected from the sphere region with a radius of $1/6$ of the matrix size, which was located in the centroid of brain, as shown in Fig. 2.4.(a). Second, initial vessel regions were segmented within the sphere region by use of a threshold of 60% of the maximum voxel value. Figure 2.4.(b) shows the initial vessel regions. By applying a region growing method to these initial vessel regions, the major vessel regions were obtained from the original MRA image, as illustrated in Fig. 2.4.(c). Figure 2.4.(d) shows the final VOI image, which was produced by 5 mm dilation and 4 mm erosion of the major vessel regions, fused with the original MRA image.



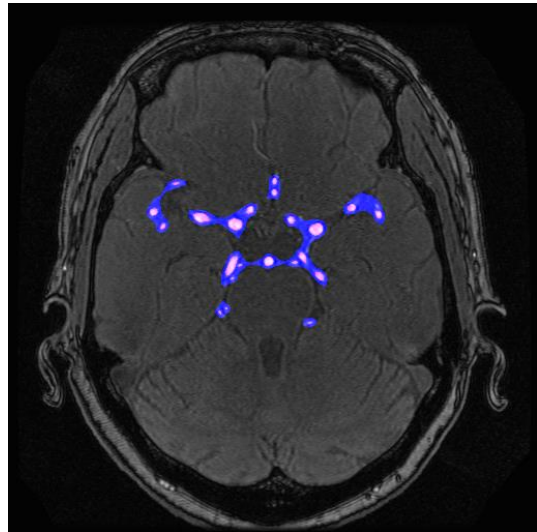
(a)



(b)



(c)



(d)

FIG. 2.4. Illustrations of extraction of a VOI in an MRA image: (a) a circle for searching for a maximum voxel value in a sphere region with a radius of $1/6$ of matrix size, (b) initial vessel regions, (c) segmented major vessel regions, and (d) a VOI region (light gray region) fused with the original MRA image.

2.2.2. A 3D blob enhancement filter

In the blob enhancement (BSE) filter [39, 44], the weight function was written as

$$w(r_s) = (r_s)^\gamma, \quad (2.1)$$

where γ controls the sharpness of selectivity for the conditions of intensity convex structures. Figure 2.5 shows the relationship between the ratio r_s and the resultant weight $w(r_s)$ for the parameter $\gamma = 0.5, 1.0$ by the conventional weight function.

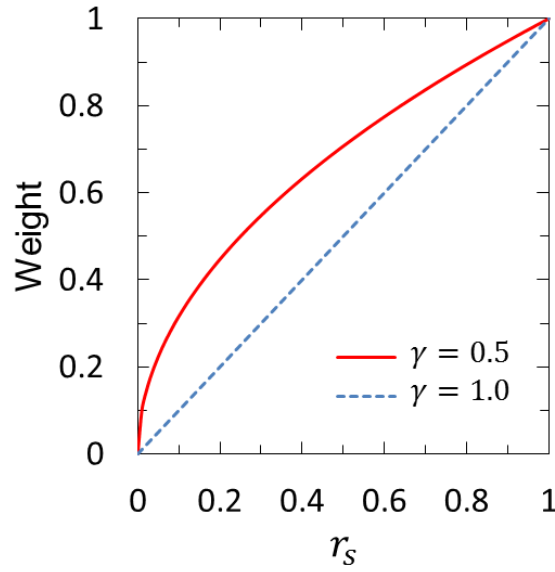


FIG. 2.5. Relationship between the ratio r_s and the resultant weight $w(r_s)$ by using a weight function with the parameter $\gamma = 0.5, 1.0$.

2.2.3. Multiple-gray-level thresholding and initial candidates selection

For identification of initial candidates, a multiple-gray-level thresholding technique was applied to the BSE images. In the technique, the corresponding threshold level and segmented volume should be increased by a small incremental volume for detecting a small aneurysm. Therefore, the incremental percentage of the area under the histogram for each threshold level was empirically determined by a fraction of a relatively small volume to the VOI, which is equivalent to the total area of the histogram. If the effective diameter of a

segmented region was greater than 1 mm or the sphericity was less than 0.6, the segmented region was considered an initial aneurysm candidate. Figure 2.6 illustrates initial candidate positions (red) on brain vessels (gray).

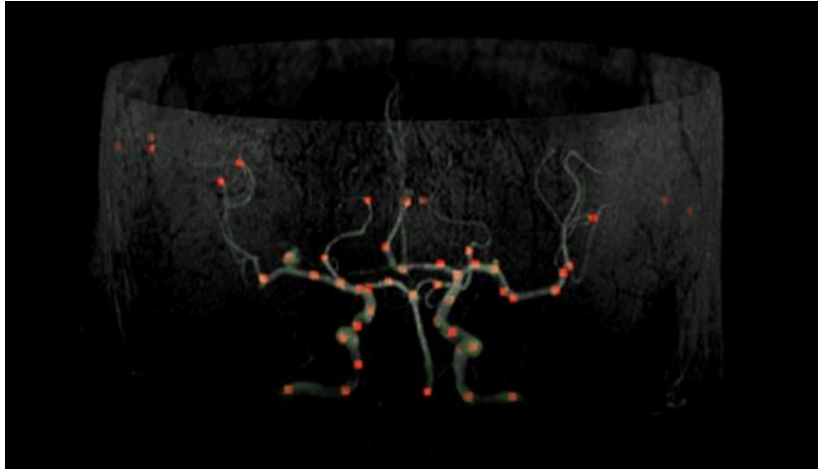


FIG. 2.6. Initial candidate positions (red points) on brain vessels (gray).

2.2.4. Segmentation of initial aneurysm regions using a region growing method

For each of the initial candidates, a candidate region was determined by applying a region-growing technique to the BSE image to obtain image features of the candidates for subsequent rule-based schemes. The region growing technique was based on detection of a large change in 5 image features, such as sphericity, effective diameter, average voxel value, which implied that the candidate region merged with its adjacent background structures or other candidates, as the candidate region grew. The region growing began at the voxel with the maximum value in the initial candidate region, and was repeated at multiple gray levels, which were decreased from each previous gray level with a decrement of 5% of the maximum voxel value. The 5 features were (1) effective diameter, which defined as a diameter of a sphere with the same volume as that of the candidate, (2) the sphericity, which defined as the fraction of the overlap volume between the candidate region and a sphere with the same volume as the candidate volume, (3) volume increasing ratio, a fraction between newly segmented volumes to the previous volume, (4) SD in the newly segmented region,

and (5) the difference between the average value of previous and newly segmented regions. Figure 2.7 illustrates a segmented candidate in (a) transverse, (b) coronal, and (c) sagittal planes.

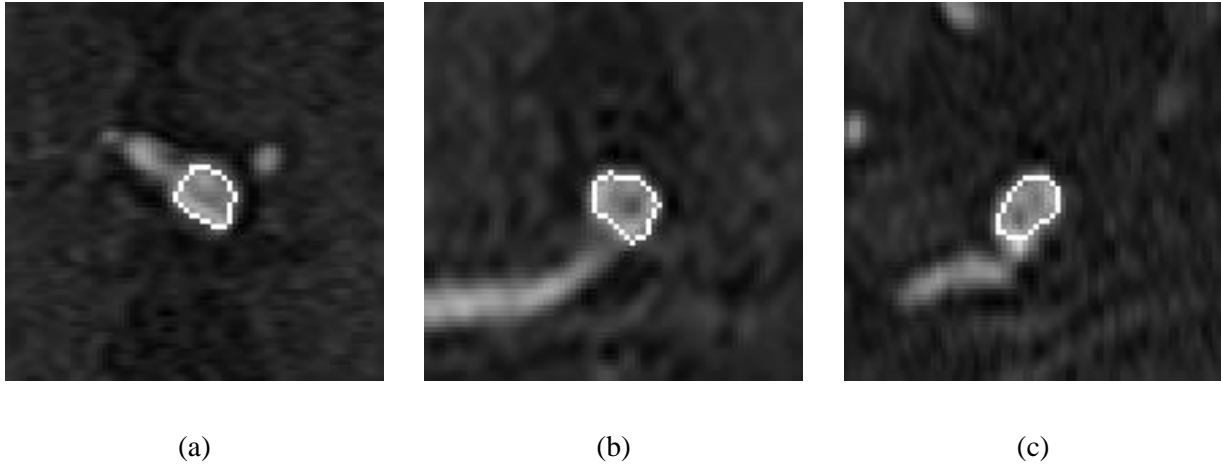


FIG. 2.7. Segmented candidate in (a) transverse, (b) coronal, and (c) sagittal planes. White lines show the contour of aneurysm.

2.2.5. Image features and FP removal

Seventeen image features including 3 morphological features and 14 gray level features for aneurysm candidates were obtained based on the regions segmented by use of a region growing technique. The following 3 morphological features were calculated in the original image.

Effective diameter:

Diameter of a sphere with the same volume as that of the candidate

Sphericity:

Fraction of the overlap volume between the candidate region and a sphere with the same volume

Segmented threshold percentage:

Percentage of the local maximum value when the candidates extracted

Furthermore, fourteen gray level features were derived from both the original MRA images and the BSE images

Average voxel value:

Average voxel value within a region of interest (ROI).

SD of voxel value:

SD of voxel values within an ROI

Average voxel value outside ROI:

Average voxel value outside the ROI

SD of voxel value outside ROI:

SD of voxel values outside the ROI

Relative contrast to average voxel value:

Difference between the maximum and minimum voxel values divided by the average voxel value within an ROI

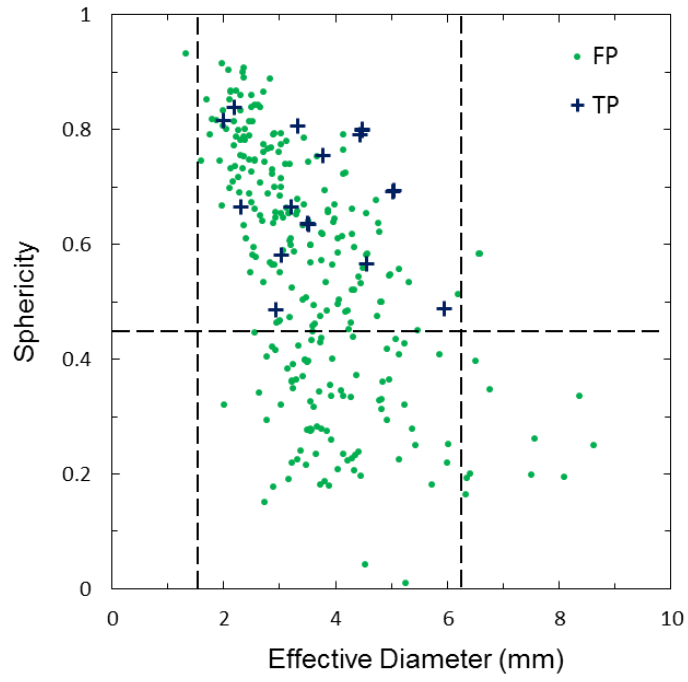
Relative difference in SD of voxel values between candidate and outside regions:

Difference in the SD of voxel values between candidate and outside regions divided by the SD within an ROI

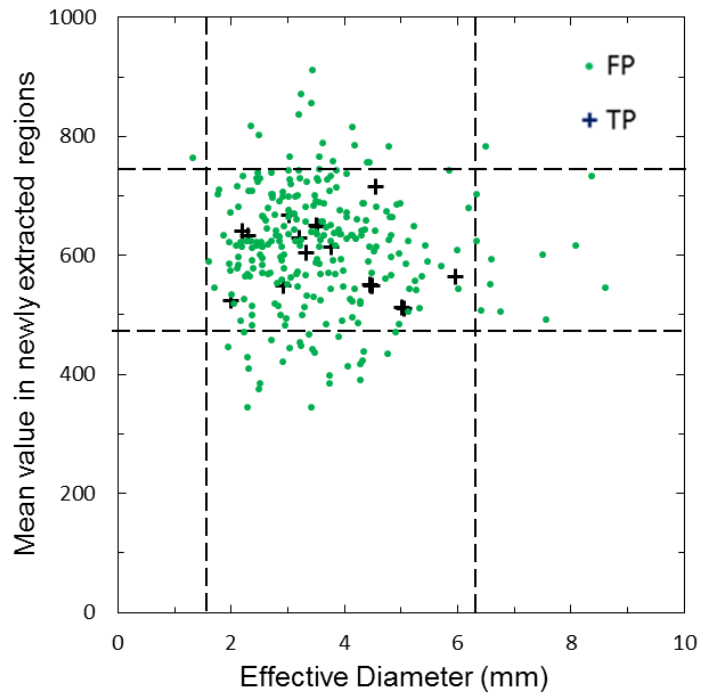
Relative difference in average voxel values between candidate and outside regions:

Difference in average voxel values between candidate and outside regions divided by the average voxel value within an ROI

In the rule-based false positives (FP) removal, FP were removed by a threshold value 5% lower than the minimum value of the sphericity for true aneurysm candidates, as shown in Fig. 2.8.(a). Simultaneously, FP were removed by threshold values 5% higher and lower than the maximum and minimum values of the other features, as illustrated in Fig. 2.8.(b).



(a)



(b)

FIG. 2.8. Scatterplots for the effective diameter with rules for FP removal (dotted lines) with (a) the sphericity, and (b) the mean value in newly extracted regions of original images.

2.3. Evaluation method

The performance of the CAD framework was evaluated by obtaining the number of FP, which is utilized to detect intracranial aneurysms with an enhancement filter that was incorporated for detection of initial candidates [50]. CAD framework was evaluated by a leave-one-patient-out test method. All patient cases except one were used for training, and the certain patient case left out was used for testing with the rule-based FP removal. This procedure was repeated for all patient cases, in order to test all cases. By changing the window size of true positives for image features which were produced from candidates for the distinction between aneurysms and FP, the free-response receiver operating characteristic (FROC) curve [51] of the CAD was produced for evaluation by comparing the relationships of the sensitivity and the number of FP per case between different methods. The number of FP of its best performance was compared to assess the capability of suppressing FP.

2.4. Results

Figure 2.9 illustrates MIP images of an original MRA and an image enhanced by a blob structure enhancement filter. Besides the aneurysm, a large number of false positives were also enhanced.

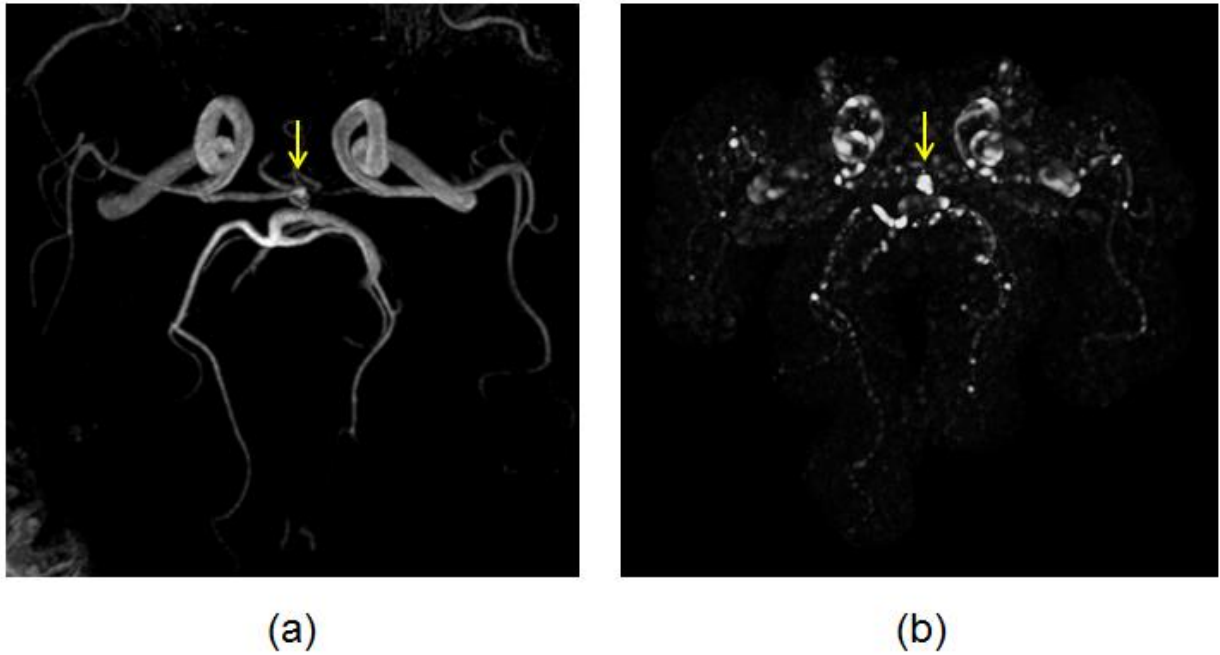


FIG. 2.9. MIP images of (a) an original MRA image, (b) an image enhanced by a blob structure enhancement filter. The aneurysm is indicated by a yellow arrow.

The automated identification scheme for detection of intracranial aneurysms was applied to 30 patients with 31 aneurysms by using the BSE filters. All aneurysms with 53.1 FPs per case were detected by the BSE filter after the initial candidate selection. Figure 2.10 shows the FROC curve of the BSE based CAD framework with a rule-based FPs removal. The number of false positives per case was 41.1 on average at a sensitivity of 87%.

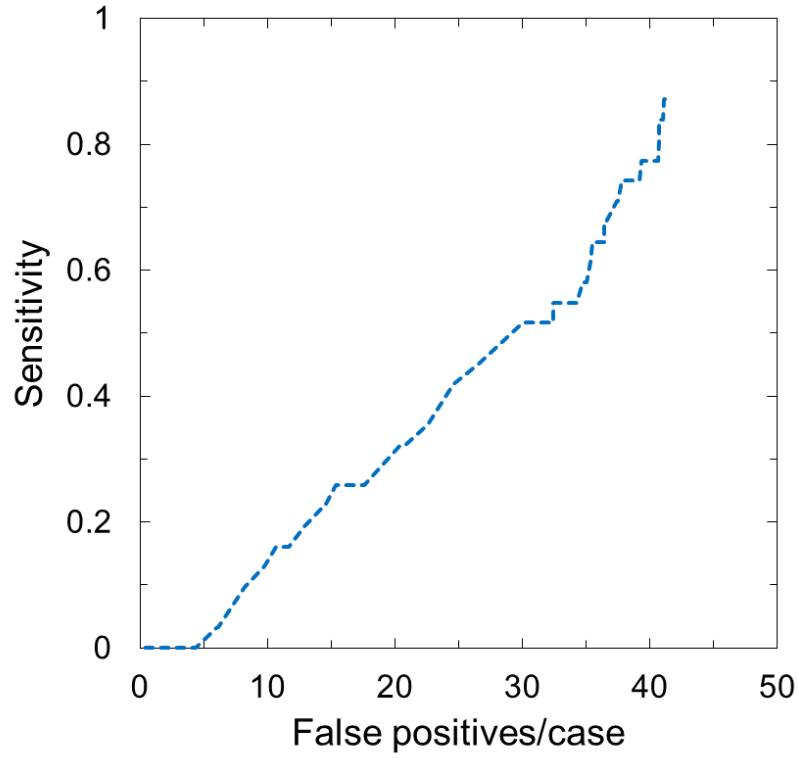


FIG. 2.10. FROC curve of the BSE based CAD framework with a rule-based FPs removal.

2.5. Problems and solutions

Since three-Tesla MRA has higher quality of visualization of intracranial aneurysms compared with 1.5 T MRA, approximation of an aneurysm to a simple sphere or blob structure can be inappropriate for the more distinct structures of aneurysms in the 3.0 T MRA images. Figure 2.11 illustrates a local intensity convex region obtained at an aneurysm in three planes, which are orthogonal to each other after a Gaussian blurring by using the MIP image with a color look up table (LUT). The local intensity convex region inside the aneurysm appeared as an ellipsoid rather than a sphere or a dot [41]. In addition, small vessels are also more clearly depicted with sharper vessel margins at 3.0 T [42,43]. Due to the detail information such as the small vessels, the good property of 3.0 T MRA images might also produce many false positives in bending or branching portions on vessels in the enhancement of aneurysm-like objects in conventional CAD schemes,

which were developed with the blob structure enhancement filter. Figure 2.12 illustrates three views of local intensity distributions in a Gaussian smoothed MRA image by using the MIP image with a color LUT. Local convex regions in the intensity space could also be obtained on the bending or branching portions on vessels (false positive structures), which were appearing as long ellipsoid structures. Figure 2.13 shows an illusion of difference of intensity distributions in an aneurysm and bending vessel portion. Aneurysms can be distinguished from bending vessels by evaluating the approximated ellipsoid structures. Therefore a new strategy is needed for enhancing aneurysms while reducing false positive contrasts on bending or branching portions on vessels by selectively enhancing the local intensity convex regions according to their modeled ellipsoid shape structures by using a quadratic approximation.

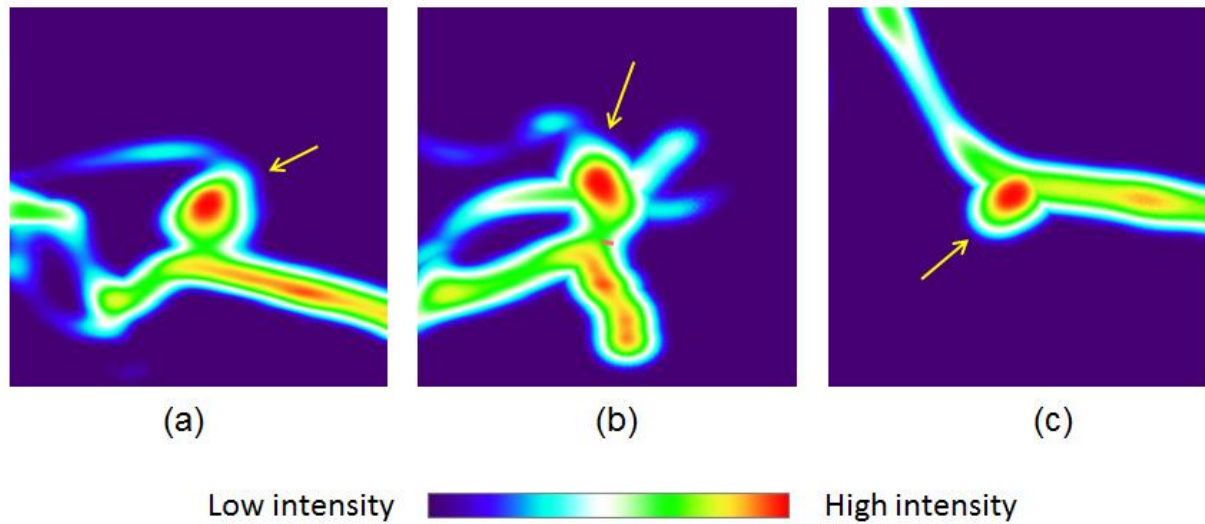


FIG. 2.11. A local intensity convex region obtained at an aneurysm in three planes, which are orthogonal to each other after a Gaussian blurring by using the MIP image with a color LUT.

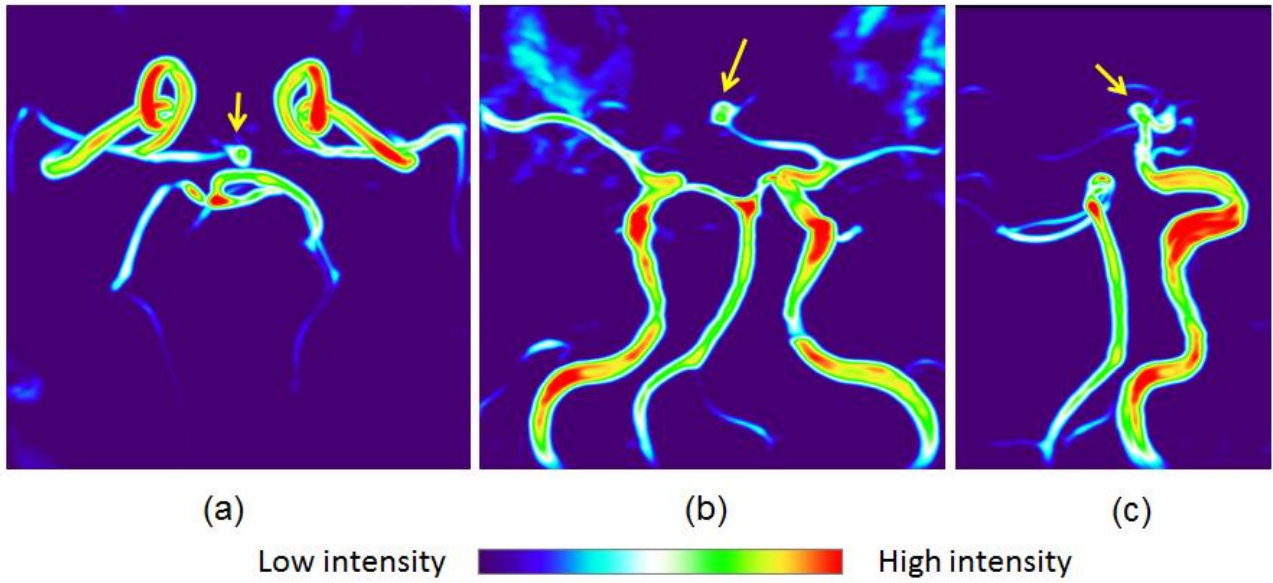


FIG. 2.12. Three views of local intensity distributions in a Gaussian smoothed MRA image by using the MIP image with a color LUT. The aneurysm is indicated by a yellow arrow.

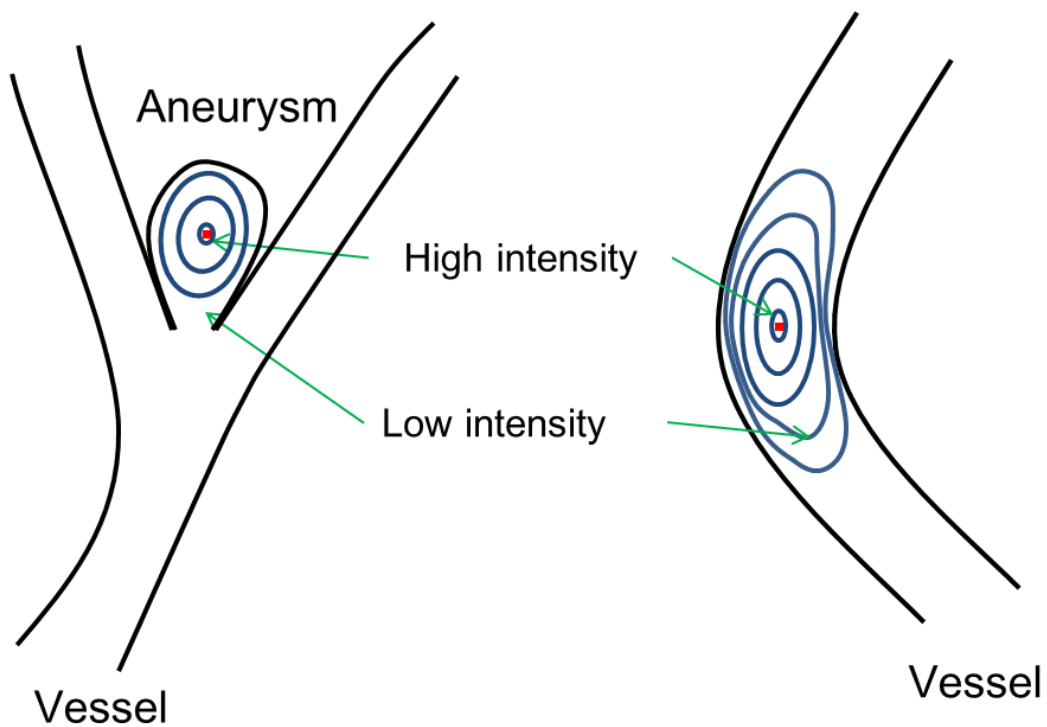


FIG. 2.13. Illusion of difference of intensity distributions in an aneurysm and bending vessel portion.

Chapter 3 Theory of an ellipsoid convex enhancement filter

This chapter includes the contents of the Ph.D. thesis “*An Ellipsoid Convex Enhancement Filter for Detection of Asymptomatic Intracranial Aneurysm Candidates in CAD Frameworks*”.

3.1. Mathematical design of ECE filter

The 3D intensity space distributions of aneurysms can be modeled by using ellipsoid and convex types of quadratic functions. Therefore, the aneurysms could be enhanced by assigning higher intensities to voxels which meet an ellipsoid and convex condition. The ellipsoid and convex condition, which could be based on eigenvalues of the Hessian matrix of the quadratic functions [45-47], was employed for development of the ellipsoid convex enhancement filter, whose theory is described below.

Let an intensity in a 3D image including convex regions be $f(x_1, x_2, x_3)$. The Taylor expansion of the local intensity $f(x_1, x_2, x_3)$ around a point $(\bar{x}_1, \bar{x}_2, \bar{x}_3)$ is written as:

$$\begin{aligned} f(x_1, x_2, x_3) &= f(\bar{x}_1, \bar{x}_2, \bar{x}_3) + \sum_{i=1}^3 \Delta x_i \frac{\partial f(\bar{x}_1, \bar{x}_2, \bar{x}_3)}{\partial x_i} \\ &+ \frac{1}{2!} \sum_{i=1}^3 \sum_{j=1}^3 \Delta x_i \Delta x_j \frac{\partial^2 f(\bar{x}_1, \bar{x}_2, \bar{x}_3)}{\partial x_i \partial x_j} + \dots, \end{aligned} \quad (3.1)$$

where $x_1 = \bar{x}_1 + \Delta x_1, x_2 = \bar{x}_2 + \Delta x_2, x_3 = \bar{x}_3 + \Delta x_3$. If the 3rd and higher order terms were ignored, the quadratic approximation of a local intensity $\hat{f}(x_1, x_2, x_3)$ can be defined by an algebra form as:

$$\begin{aligned} \hat{f}(x_1, x_2, x_3) &= f(\bar{x}_1, \bar{x}_2, \bar{x}_3) + \nabla f(\bar{x}_1, \bar{x}_2, \bar{x}_3) \begin{pmatrix} x_1 - \bar{x}_1 \\ x_2 - \bar{x}_2 \\ x_3 - \bar{x}_3 \end{pmatrix} \\ &+ \frac{1}{2!} \left(\begin{pmatrix} x_1 - \bar{x}_1 \\ x_2 - \bar{x}_2 \\ x_3 - \bar{x}_3 \end{pmatrix}, \mathbf{H} \begin{pmatrix} x_1 - \bar{x}_1 \\ x_2 - \bar{x}_2 \\ x_3 - \bar{x}_3 \end{pmatrix} \right), \end{aligned} \quad (3.2)$$

where $\nabla = \left(\frac{\partial}{\partial x_1}, \frac{\partial}{\partial x_2}, \frac{\partial}{\partial x_3} \right)$, and

$$\mathbf{H} = \begin{pmatrix} \frac{\partial^2 f(\bar{x}_1, \bar{x}_2, \bar{x}_3)}{\partial x_1^2} & \frac{\partial^2 f(\bar{x}_1, \bar{x}_2, \bar{x}_3)}{\partial x_1 \partial x_2} & \frac{\partial^2 f(\bar{x}_1, \bar{x}_2, \bar{x}_3)}{\partial x_1 \partial x_3} \\ \frac{\partial^2 f(\bar{x}_1, \bar{x}_2, \bar{x}_3)}{\partial x_2 \partial x_1} & \frac{\partial^2 f(\bar{x}_1, \bar{x}_2, \bar{x}_3)}{\partial x_2^2} & \frac{\partial^2 f(\bar{x}_1, \bar{x}_2, \bar{x}_3)}{\partial x_2 \partial x_3} \\ \frac{\partial^2 f(\bar{x}_1, \bar{x}_2, \bar{x}_3)}{\partial x_3 \partial x_1} & \frac{\partial^2 f(\bar{x}_1, \bar{x}_2, \bar{x}_3)}{\partial x_3 \partial x_2} & \frac{\partial^2 f(\bar{x}_1, \bar{x}_2, \bar{x}_3)}{\partial x_3^2} \end{pmatrix}. \quad (3.3)$$

\mathbf{H} is called a Hessian matrix.

By using linear translation and scaling, the local intensity $\hat{f}(x_1, x_2, x_3)$ can be expressed by the following equation:

$$\hat{f}(x_1, x_2, x_3) = (\mathbf{x}, \mathbf{H}\mathbf{x}), \quad (3.4)$$

where a relative position vector $\mathbf{x} = \begin{pmatrix} x_1 - \bar{x}_1 \\ x_2 - \bar{x}_2 \\ x_3 - \bar{x}_3 \end{pmatrix}$.

The Hessian matrix can be diagonalized by an orthonormal matrix \mathbf{U} as:

$$\mathbf{D} = \mathbf{U}^T \mathbf{H} \mathbf{U}, \quad (3.5)$$

where $\mathbf{D} = \begin{pmatrix} \lambda_1 & & \\ & \lambda_2 & \\ & & \lambda_3 \end{pmatrix}$, in which $\lambda_1, \lambda_2, \lambda_3$ ($\lambda_1 \geq \lambda_2 \geq \lambda_3$) are the first, second, and third eigenvalues of the Hessian matrix, respectively, and $\mathbf{U} = (\mathbf{u}_1 \mathbf{u}_2 \mathbf{u}_3)$, in which $\mathbf{u}_1, \mathbf{u}_2, \mathbf{u}_3$ are unit eigenvectors.

If the relative position vector \mathbf{x} can be expressed by a linear combination of the transformed relative position vector $\mathbf{x}' = \mathbf{U}^T \mathbf{x} = (x'_1 - \bar{x}'_1 \ x'_2 - \bar{x}'_2 \ x'_3 - \bar{x}'_3)^T$ by using the following relationship:

$$\mathbf{x} = \mathbf{U} \mathbf{x}'. \quad (3.6)$$

Equation (3.4) can be transformed into:

$$\begin{aligned} \hat{f}(x'_1, x'_2, x'_3) &= (\mathbf{U} \mathbf{x}', \mathbf{H} \mathbf{U} \mathbf{x}') = (\mathbf{x}', \mathbf{U}^T \mathbf{H} \mathbf{U} \mathbf{x}') = (\mathbf{x}', \mathbf{D} \mathbf{x}') \\ &= \lambda_1 (x'_1 - \bar{x}'_1)^2 + \lambda_2 (x'_2 - \bar{x}'_2)^2 + \lambda_3 (x'_3 - \bar{x}'_3)^2. \end{aligned} \quad (3.7)$$

The local intensity function $\hat{f}(x'_1, x'_2, x'_3)$ is convex when $0 \gg \lambda_1 \geq \lambda_2 \geq \lambda_3$, and it is concave when $\lambda_1 \geq \lambda_2 \geq \lambda_3 \gg 0$, and it is hyperbolic paraboloid when at least one of eigenvalues is opposite sign to the

other eigenvalues. Therefore, the ellipsoid and convex local points can be detected by evaluating the eigenvalues of the Hessian matrix.

The ellipsoid and convex points would satisfy a condition that $0 \gg \lambda_1 \geq \lambda_2 \geq \lambda_3$ and Equation (3.7) can be transformed into an ellipsoid form as follows:

$$\hat{f}(x'_1, x'_2, x'_3) = - \left(\frac{(x'_1 - \bar{x}'_1)^2}{\left(\sqrt{\frac{1}{|\lambda_1|}}\right)^2} + \frac{(x'_2 - \bar{x}'_2)^2}{\left(\sqrt{\frac{1}{|\lambda_2|}}\right)^2} + \frac{(x'_3 - \bar{x}'_3)^2}{\left(\sqrt{\frac{1}{|\lambda_3|}}\right)^2} \right). \quad (3.8)$$

For a certain $\hat{f}(x_1, x_2, x_3) = -k, k > 0$, this local convex point can be approximated by an ellipsoid function:

$$1 = \frac{(x'_1 - \bar{x}'_1)^2}{\left(\sqrt{\frac{k}{|\lambda_1|}}\right)^2} + \frac{(x'_2 - \bar{x}'_2)^2}{\left(\sqrt{\frac{k}{|\lambda_2|}}\right)^2} + \frac{(x'_3 - \bar{x}'_3)^2}{\left(\sqrt{\frac{k}{|\lambda_3|}}\right)^2}. \quad (3.9)$$

The ratio of the semi-minor axis to the semi-major axis of the ellipsoid function can be calculated by using the ratio of eigenvalues:

$$\frac{\text{semiminor axis}}{\text{semimajor axis}} = \frac{\sqrt{\frac{k}{|\lambda_3|}}}{\sqrt{\frac{k}{|\lambda_1|}}} = \sqrt{\frac{|\lambda_1|}{|\lambda_3|}}. \quad (3.10)$$

This ratio, ranging from 0 to 1, can be used to evaluate the shape of the modeled ellipsoid.

In this study, the Hessian matrix at each coordinate (x, y, z) in a Gaussian smoothed MRA image $I(x, y, z)$ is given by

$$\mathbf{H} = \begin{pmatrix} I_{xx}(x, y, z) & I_{xy}(x, y, z) & I_{xz}(x, y, z) \\ I_{yx}(x, y, z) & I_{yy}(x, y, z) & I_{yz}(x, y, z) \\ I_{zx}(x, y, z) & I_{zy}(x, y, z) & I_{zz}(x, y, z) \end{pmatrix}, \quad (3.11)$$

where

$$I_{x^i y^j z^k}(x, y, z; \sigma) = \left(\frac{\partial^2}{\partial x^i \partial y^j \partial z^k} G_\sigma(x, y, z) \right) * I(x, y, z), \quad (3.12)$$

where $G_\sigma(x, y, z)$ represents a Gaussian filter with a standard deviation (SD) σ , $*$ represents convolution,

and i, j, k are positive integers, which satisfy $i + j + k = 2$. In order to detect intensity convex structures with different sizes, Gaussian filters with multiple sizes, which were determined according to the range of the longest diameters of aneurysms, were introduced in this study.

Intensity convex structures could be selectively enhanced by an enhancement function:

$$S_{convex} = |\lambda_3| \cdot w(r_s), \quad (3.13)$$

where $r_s = \frac{|\lambda_1|}{|\lambda_3|}$ represents the ratio of shortest diameter to the longest diameter of the intensity convex structures, and was considered the ratio of semi-minor axis to the semi-major axis of the approximated ellipsoid shape. The term $w(r_s)$ is the weight affecting the contrast curve in terms of the ratio of the shortest diameter to the longest diameter for the intensity convex structures.

In this study, a sigmoid function was introduced in the weight function to selectively enhance the round ellipsoid shapes with high ratio of the shortest diameter to the longest diameter and suppress long ellipsoid shapes. The modified weight function is defined as

$$w(r_s) = \frac{1}{1 + e^{-\alpha(r_s - \tau)}}, \quad (3.14)$$

where α and τ control the sharpness and range of selectivity for the conditions of intensity convex structures, respectively, in terms of the ratio of the shortest diameter to the longest diameter. Figure 3.1 shows the relationship between the ratio r_s and the resultant weight $w(r_s)$ with the parameters $\alpha = 10, \tau = 0.5$ by using the proposed sigmoid based weight function.

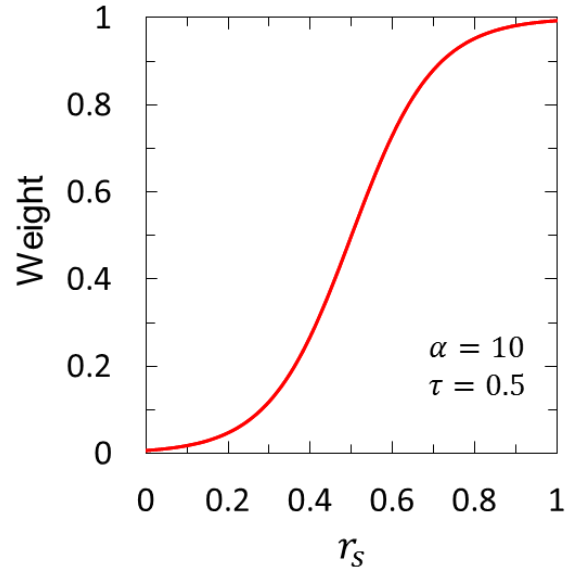


FIG. 3.1. Relationship between the ratio r_s and the resultant weight $w(r_s)$ by using the proposed sigmoid based weight function with the parameters $\alpha = 10$ and $\tau = 0.5$.

3.2. Evaluation of ECE filter

3.2.1 Gaussian ellipsoid models of various convex regions for evaluation

For comparison of the conventional and proposed ECE filters and determination of parameter set in the ECE filter, a group of Gaussian ellipsoid models were introduced in this study. The ellipsoid models have shortest, longest and middle diameters in x, y and z directions, respectively. According to the real sizes of small aneurysms used in this study, the longest diameters d_l of the ellipsoid are defined as 1.4 to 6.3 mm with a voxel size of 0.35 mm. The shortest diameter d_s and middle diameter d_m were defined as $d_s = d_l \times \left(1 - 0.9 \times \frac{i}{n}\right)$ and $d_m = d_l \times \left(1 - 0.45 \times \frac{i}{n}\right)$, where n and i are the amount and index numbers of models with a longest diameter of d_l .

Voxel values of each model were determined by a Gaussian function:

$$G(x, y, z) = ke^{-\frac{(x-x_c)^2}{2\sigma_x^2} - \frac{(y-y_c)^2}{2\sigma_y^2} - \frac{(z-z_c)^2}{2\sigma_z^2}} \quad (3.15)$$

where x, y, z represent the voxel number in a Gaussian ellipsoid model with a center point of (x_c, y_c, z_c) and k is the maximum voxel value at the center point, which was set to be 100. The SDs in x, y and z directions were defined as $\sigma_x = d_s/4$, $\sigma_y = d_l/4$ and $\sigma_z = d_m/4$, respectively, for making the range of diameters covered by the Gaussian distribution intensity.

Figure 3.2 illustrates Gaussian ellipsoid models with various longest diameters (1.4 to 6.3 mm) and ratios (0.1 to 1.0) of the shortest diameters to the longest diameters. The yellow points represent the distribution of 31 real aneurysms that used in this study. Most aneurysm structures have ratios of the shortest diameters to the longest diameters higher than 0.4. On the other hand, some false positive structures might cause long elliptical local convex regions in the intensity space.

In order to obtain a proper parameter set for enhancement of aneurysms, different parameter sets were employed and compared in an evaluation by using the Gaussian ellipsoid models. To fit the parameter set for the discrimination in enhancement of aneurysms or suppression of false positive structures, response curves of the ECE filter to Gaussian ellipsoid models with different parameter sets were obtained. The proper parameter set should provide a sharpness of selectivity as well as a suitable soft discrimination for Gaussian ellipsoid models based on the ratio of the shortest diameter to the longest diameter according to the distribution of real aneurysms in the data base.

Based on the clinical cases used in this study, the Gaussian ellipsoid models were divided into two groups of aneurysms models and false positive models by a threshold of the ratio of the shortest diameter to the longest diameter, which was set to be 0.4. The performances of the ECE filters were evaluated in terms of enhancement of the aneurysms models and suppressing of the false positive models.

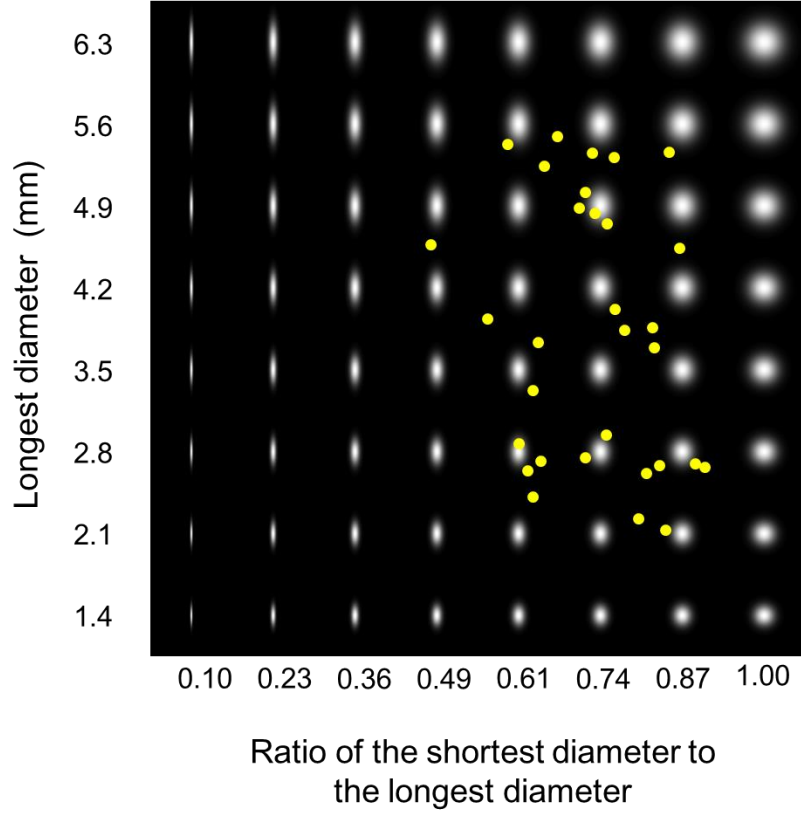


FIG. 3.2. Gaussian ellipsoid models with various longest diameters and ratios of the shortest diameters to the longest diameters. Yellow points represent the distribution of 31 real aneurysms that used in this study.

3.2.2 A conventional method for enhancement of convex regions

A conventional approach [39,44] for convex region enhancement was used for evaluation of the ECE filter by comparing the performance of enhancing aneurysms structures and suppressing false positive structures using Gaussian ellipsoid models and a simple CAD framework for 3.0 T MRA images.

In the conventional approach, the weight function was written as

$$w(r_s) = (r_s)^\gamma, \quad (3.16)$$

where γ controls the sharpness of selectivity for the conditions of intensity convex structures. Figure 2.5 shows the relationship between the ratio r_s and the resultant weight $w(r_s)$ for the parameter $\gamma = 0.5, 1.0$ by the conventional weight function.

Gaussian filter sizes for the ECE filters were determined based on the size range of the 31 aneurysms. Three σ values ($4\sigma = 1.4, 4.2, \text{ and } 7.0 \text{ mm}$) were used in this study. A parameter γ of 0.5 was used in the conventional filter according to the past studies [28,29]. The parameters α and τ in the ECE filter were determined by evaluating the enhancement of Gaussian ellipsoid models of various convex regions.

3.3. Results

Figure 3.3 illustrate (a) ECE filter enhance Gaussian ellipsoids, and (b) the center intensity of each Gaussian model. Response curves were made as relationships between the average intensity and standard deviation at a center point of each enhanced model and the ratio d_s/d_l of the shortest diameter to the longest diameter, i.e. average intensity and standard deviation in each column in Fig. 3.3(b).

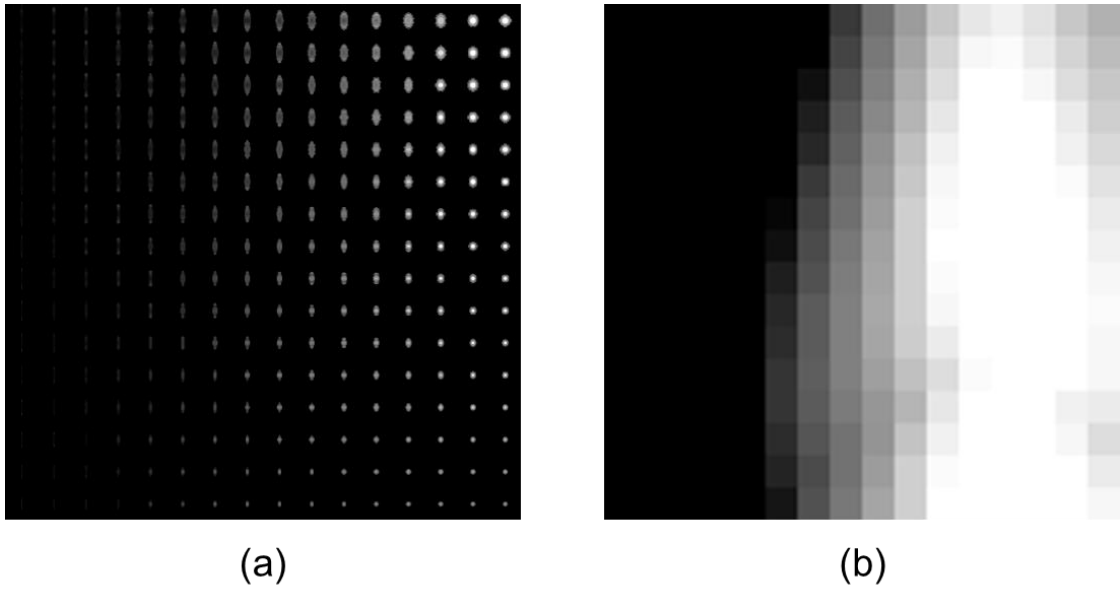


FIG. 3.3. Illustrations of (a) ECE filter enhance Gaussian ellipsoids, and (b) the center intensity of each Gaussian model.

The Gaussian ellipsoid models were enhanced by the ECE filter with combinations of three α values (5, 10 and 15) and three τ values (0.25, 0.50 and 0.75). A contrast changing, which represent the changing

of sharpness of selectivity, could be obtained among different α value images, and a boundary changing could be obtained among different τ values images. Figure 3.4 shows response curves of Gaussian ellipsoid models to the ECE filter for different parameter sets. By using parameter sets of different α values with $\tau = 0.50$, which is shown in Fig. 3.4.(a), all response curves passed through a certain point, based on the fact that the center of the boundary between enhancement and suppression was set by determining the ratio of the shortest diameter to the longest diameter. A large α value could provide sharp slope in the response curve, meaning a clear discriminant of the ECE filter for the intensity convex structures. On the other hand, by using parameter sets of different τ values with $\alpha = 10$, which is shown in Fig. 3.4.(b), all response curves have a certain pattern of slope, and appearing to be similar curves placed in different positions. Thus, the condition of the ratio of the shortest diameter to the longest diameter could be used as a control option for the selective intensity convex enhancement. By comparing these results with the distribution of ratio of shortest to longest diameters from real aneurysms as shown in Fig. 11, the parameter set for the enhancement of aneurysms was set as $\alpha = 10$ and $\tau = 0.5$ for the aneurysms used in this study.

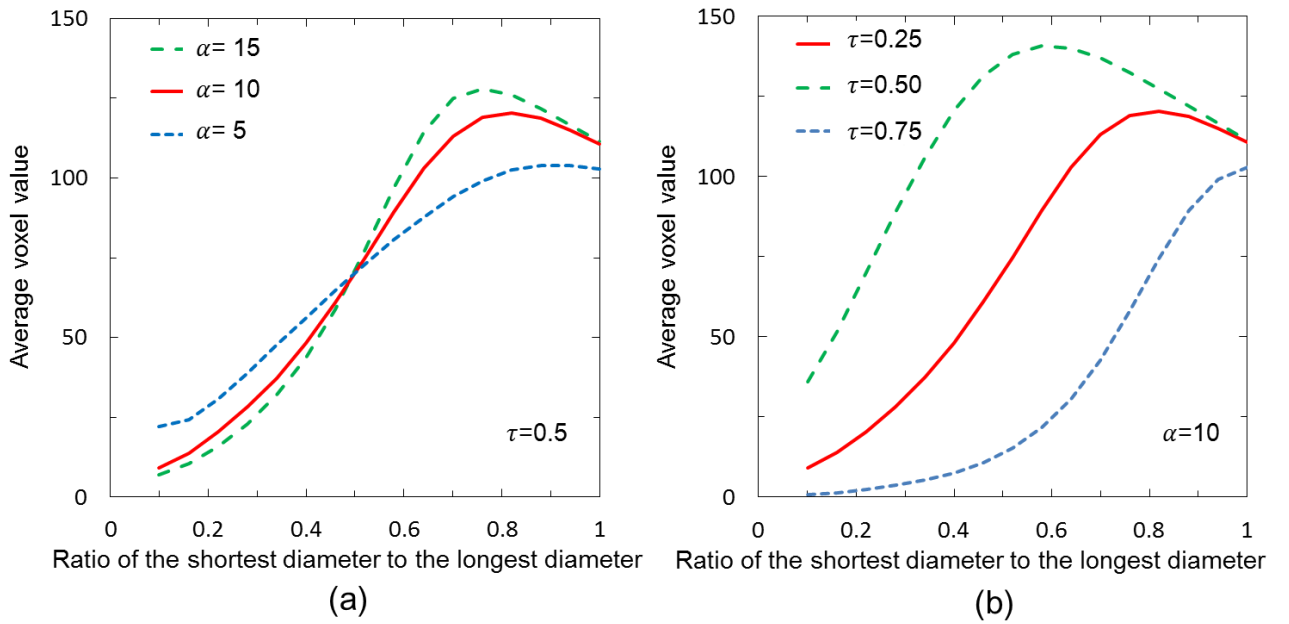


FIG. 3.4. Response curves of Gaussian ellipsoid models to the ECE filter for different parameter sets.

Figure 3.5 shows enhanced Gaussian ellipsoid models using the ECE filter and the conventional filter, with a relationship between the longest diameter and the ratio of the shortest diameter to the longest diameter. Yellow points represent data of 31 real aneurysms. By applying the ECE filter, aneurysm models were enhanced and false positive models were suppressed. However, by applying the conventional filter, both aneurysm models and false positive models were enhanced without substantial differences. Figure 3.6 illustrates the response curves of Gaussian ellipsoid models to the conventional and ECE filters. For the ellipsoid models with a ratio of the shortest diameter to the longest diameter larger than 0.8, they could be equivalently enhanced by two kinds of filter. Gaussian models with the ratio of the shortest diameter to the longest diameter lower than 0.40 were significantly suppressed by the ECE filter. Ellipsoid models with the ratio close to 0.1 were suppressed by both conventional and ECE filters. However, similar as the weight function curves in Fig. 8, the suppression using the proposed ECE filter was more significant than that using the conventional filter.

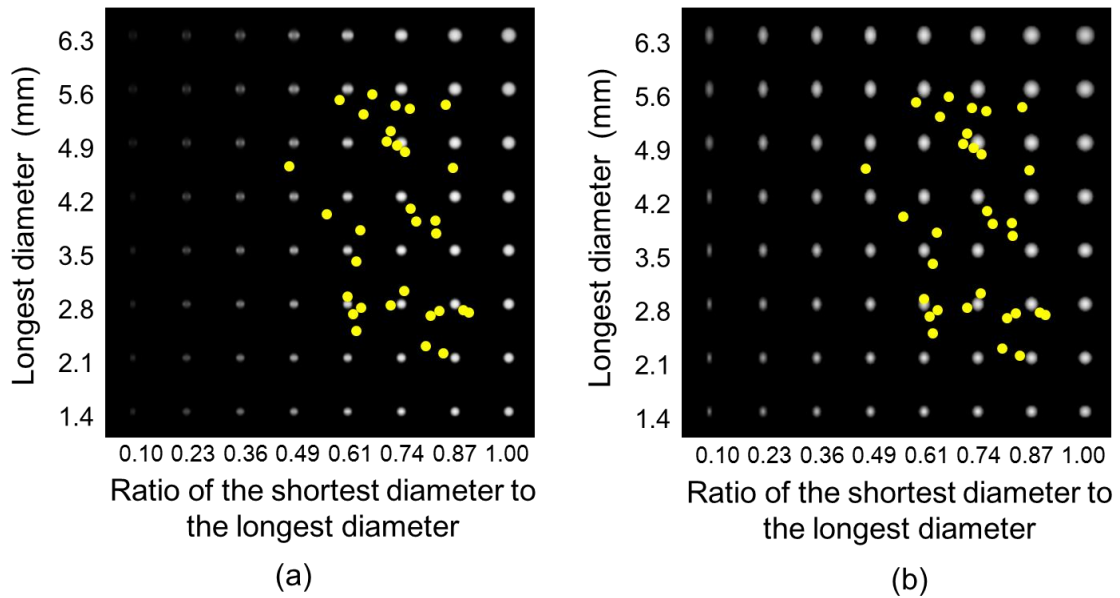


FIG. 3.5. Enhancement of Gaussian models using (a) the ECE filter, and (b) the conventional filter, with a relationship between the longest diameter and the ratio of the shortest diameter to the longest diameter. Yellow points represent data of 31 real aneurysms.

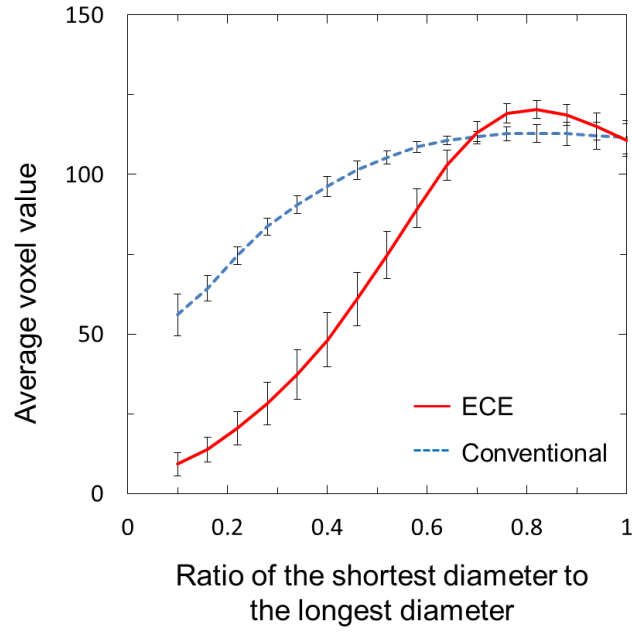


FIG. 3.6. Response curves of Gaussian ellipsoid models to the conventional (blue dashed line) and ECE (red solid line) filters. Error bars represent standard deviations.

Figure 3.7 illustrates a MIP image of the ECE filter enhanced 3.0 T MRA image with the same original image shown in Fig. 2.9.(a). The aneurysm was indicated by a yellow arrow in each image. Compared with Fig. 2.9.(b), the false positive structures were enhanced by the conventional filter but unenhanced by the ECE filter, for its long ellipsoid convex intensity distribution after Gaussian smoothing.

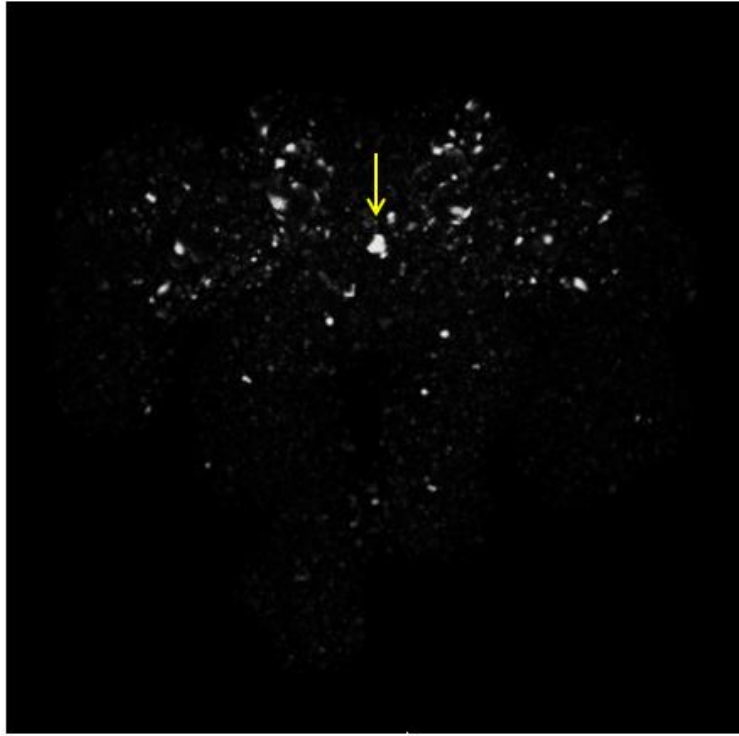


FIG. 3.7. A MIP image of the ECE filter enhanced 3.0 T MRA image with the same original image shown in Fig. 2.9. The aneurysm is indicated by a yellow arrow.

The automated identification scheme for detection of intracranial aneurysms was applied to 30 patients with 31 aneurysms by using the ECE and conventional filters. All aneurysms with 31.8 FPs per case were detected by the ECE filter, and 26 aneurysms (83.9% of all) with 53.1 FPs per case were detected by the conventional filter after the initial candidate selection. Figure 3.8 shows the FROC curves of the conventional and ECE filters with a rule-based FPs removal. The number of false positives per case was decreased from 41.1 to 22.8 on average at a sensitivity of 87% by using the ECE filter instead of the conventional filter. Figure 3.9 shows the final candidates outputted from the CAD framework. The aneurysm was detected and segmented, which is indicated by a yellow arrow.

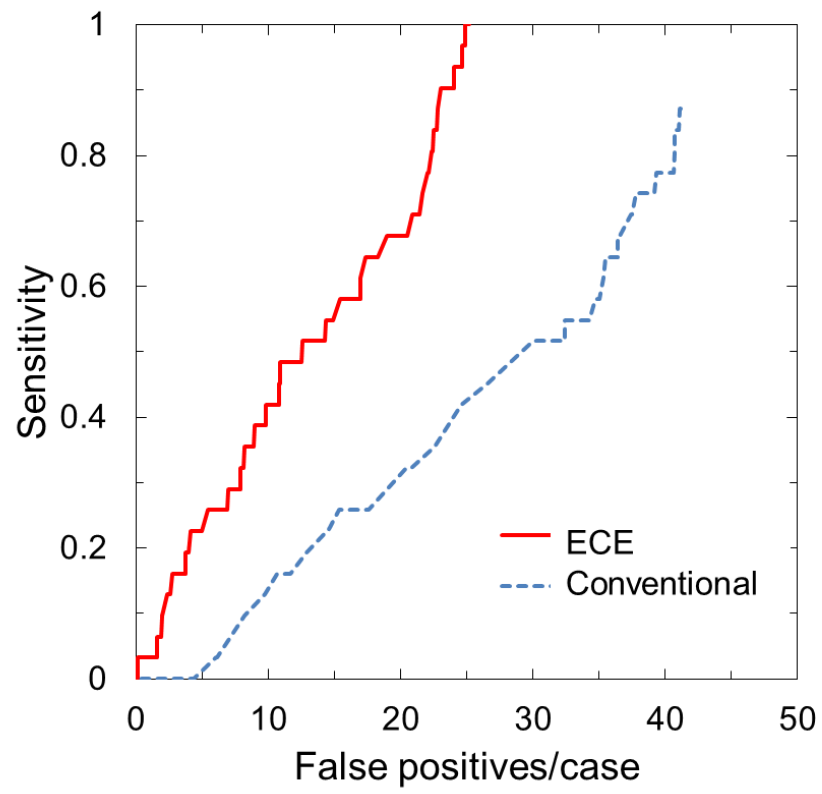


FIG. 3.8. FROC curves of the conventional and ECE filters with a rule-based FPs removal.

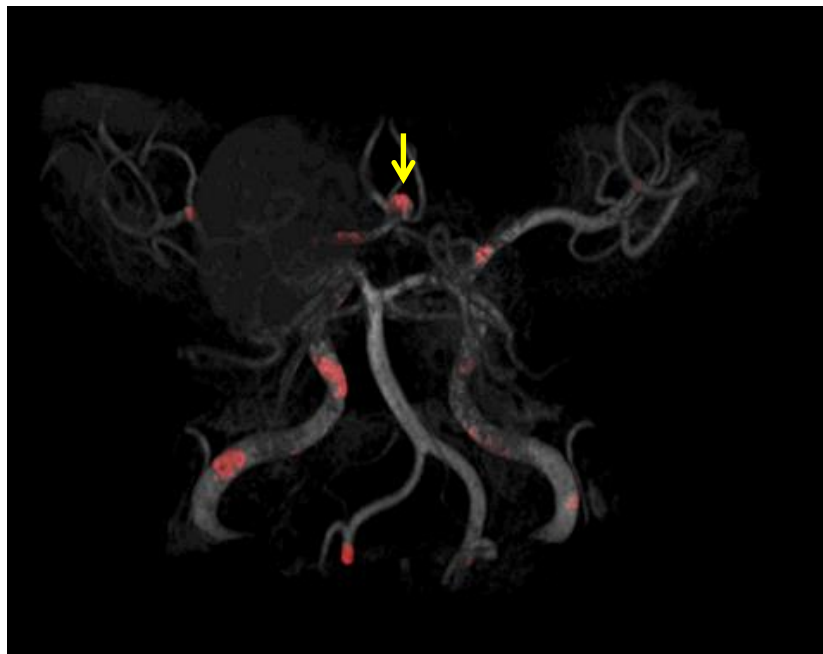


FIG. 3.9. Final candidate regions (red) on vessels. The aneurysm is indicated by a yellow arrow.

3.4. Discussion

The results of Gaussian ellipsoid models test showed a significant advantage of the proposed ECE filter in suppressing false positives long ellipsoid models. Figure 3.5 illustrates similar contrasts of enhanced Gaussian ellipsoid models with the ratios the shortest diameter to the longest diameter larger than 0.74 using the ECE and conventional filters. However, these figures indicate evident lower contrasts for the Gaussian ellipsoid models with the ratios of the shortest diameter to the longest diameter lower than 0.36 by using the ECE filter compared with the conventional filter. By comparing the response curves of the ECE and conventional filters in Fig. 3.6, the average contrast of the center values was reduced by 51.4% for Gaussian ellipsoid models of false positives with the ratio of the shortest diameter to the longest diameter less than 0.4. Meanwhile, the average contrast of the center values was increased by 1.8% for the Gaussian ellipsoid models with the ratio of the shortest diameter to the longest diameter larger than 0.6, i.e. aneurysm shape models.

Because the ECE filter was designed to detect aneurysms with longest diameters less than 7 mm with localized intensity convex regions, some aneurysms might be unenhanced for large volume or local intensity concave region caused by the slow blood flow in the center of the aneurysm. However, as mentioned in Introduction section, the large aneurysms could be easily detected by radiologists. Those large aneurysms can be obtained by using the ECE filter with larger Gaussian filters at the cost of prolonging the calculation time from 2 min 57 sec to 8 min 4 sec on average for enhancing the images. Therefore, we focused on detection of aneurysms smaller than 7 mm in this study.

Our databases included a variety of aneurysms in terms of the size, location, shape, and the gender and age of the patients. However, because all cases in this study were collected from a certain institution with a specific magnetic resonance imaging scanner, the results would possibly depend on the acquisition sequence and/or the imaging method. Therefore, the proposed ECE filter should be tested on a database with a

diversity of image acquisition machines. For adaptation of multiple image qualities, some improvement could be necessary, such as intensity inhomogeneity correction [52]. Fortunately, since the two parameters can be determined according to the size distribution of real aneurysms in other databases, the proposed ECE filter can be easily modified for other data sets.

The proposed ECE filter has an advantage in suppressing false positive structures compared with the conventional filter, for its capability of selectively enhancing the local intensity convex regions according to their modeled ellipsoid shape structures by using the quadratic approximation, compared with the simple similarity index to a sphere or dot structure in the conventional filter. The discrimination between aneurysm liked structures and false positive long ellipsoid structures could be obtained from the data base of measured aneurysms and controlled by the two parameters α and τ for a controllable sharpness of selectivity as well as the inflection point between enhancement and suppressing.

We have proposed an ellipsoid convex enhancement filter, by which the average contrast for false positive models was reduced by 51.4% compared with the conventional filter. The ECE filter would be useful for boosting the performance of the CAD framework of asymptomatic intracranial aneurysms by providing a higher contrast between aneurysms and false positives such as bending or branching portions on vessels.

Chapter 4 Conclusions

In this thesis, we proposed an ellipsoid convex enhancement filter, which was mathematically designed to enhance various convex regions in the intensity space such as convex aneurysms, in which the ratio of the shortest and longest diameters for aneurysms corresponds to the ratio of reciprocals of the square roots of the first and third eigenvalues of a Hessian matrix. With this proposed filter, we developed a CAD framework, which could selectively provide aneurysm candidate for the radiologist in detection of asymptomatic intracranial aneurysm.

In Chapter 1, we introduced the background of diagnosis of asymptomatic intracranial aneurysm. We explained our motivation based on the problems of conventional methods.

In Chapter 2, we introduced a CAD framework of asymptomatic intracranial aneurysms based on the BSE filter.

In Chapter 3, we introduced the theory of our proposed ellipsoid convex enhancement filter, and evaluated it by using Gaussian ellipsoid models. The average contrast for false positive models was reduced by 51.4% using the ECE filter, compared with the conventional filter for the convex regions with ratios of the shortest and longest diameter less than 0.4. The result showed that the ECE filter would be useful for boosting the performance of the CAD framework of asymptomatic intracranial aneurysms by providing a higher contrast between aneurysms and false positives such as bending or branching portions on vessels.

Acknowledgement

I would like to express my deep gratitude to Prof. Dr. Hidetaka Arimura, Faculty of Medical Sciences, Kyushu University, my research supervisors, for his helpful invariable suggestions, patient guidance, enthusiastic encouragement and useful critiques of this research work.

I express special thanks to Prof. Dr. Yukunori Korogi and Prof. Dr. Shingo Kakeda, Department of Radiology, University of Occupational & Environmental Health School of Medicine, for invaluable comments from the clinical point of view.

I would like to gratefully thank Prof. Dr. Makoto Sasaki and Prof. Dr. Fumio Yamashita, Faculty of Medical Sciences, Division of Ultrahigh Field MRI, Institute for Biomedical Sciences, Iwate Medical University, for their guidance and helpful discussion on MR imaging processing.

Moreover, my special thanks are given to all faculty members of Division of Medical Quantum Science, Department of Health Sciences, Faculty of Medical Sciences, Kyushu University and all members of Arimura's laboratory in Kyushu University for their great contribution to this study.

Finally, I note that I was a recipient of Otsuka Toshimi Scholarship Foundation during this study. Meanwhile, this work was supported by Japan Society for the Promotion of Science Grant-in-Aid for JSPS fellows and partially supported by New Energy and Industrial Technology Development Organization (NEDO).

References

- [1] I. Chatziprodromou, A. Tricoli, D. Poulikakos, and Y. Ventikos, “Haemodynamics and wall remodelling of a growing cerebral aneurysm: a computational model,” *J. Biomech.* **40**, 412-426 (2007).
- [2] D.O. Wiebers, J.P. Whisnant, and W.M. O’Fallon, “The Natural History of Unruptured Intracranial Aneurysms,” *N. Engl. J. Med.* **304** 696-698 (1981).
- [3] J.M. Wardlaw, and P.M. White, “The detection and management of unruptured intracranial aneurysms,” *Brain* **123**, 205-221 (2000).
- [4] W.G. Eckert, and S.H. James, *Interpretation of bloodstain evidence at crime scenes*. (CRC press, Boca Raton, 1998).
- [5] http://www.hopkinsmedicine.org/healthlibrary/conditions/nervous_system_disorders/cerebral_aneurysm_85,P08772/
- [6] P.M. White, E.M. Teasdale, J.M. Wardlaw, and V. Easton, “Intracranial aneurysms: CT angiography and MR angiography for detection prospective blinded comparison in a large patient cohort,” *Radiol.* **219**, 739 – 749 (2001).
- [7] A. Doerfler, W. Becker, I. Wanke, S. Goericke, N. Oezkan, and M. Forsting, “Multimodal imaging in the elastase-induced aneurysm model in rabbits: a comparative study using serial DSA, MRA and CTA,” *Fortschr Röntgenstr* **176**, 590-596 (2004).
- [8] K. Hashi, 50th anniversary international symposium of northern-region medicine & health sciences, Sapporo Medical University, Hokkaido, Japan
- [9] D.O. Wiebers and International Study of Unruptured Intracranial Aneurysms Investigators, “Unruptured intracranial aneurysms: natural history, clinical outcome, and risks of surgical and endovascular treatment,” *Lancet* **362**, 103-110 (2003).
- [10] R.R. Lall, C.S. Eddleman, B.R. Bendok, and H.H. Batjer, “Unruptured intracranial aneurysms and the assessment of rupture risk based on anatomical and morphological factors: sifting through the sands of data.” *Neurosurg. Focus* **26**, E2 (2009).
- [11] H. Arimura, Research and Development of Computer-aided Diagnostic System in the Field of Neuroradiology, 医学物理, 教育講演資料, **28**, Supplement 1, pp.1-20 (2008).
- [12] S. Wang, W. Wu, “A Novel Method for Magnetic Resonance Brain Image Classification based on Adaptive Chaotic PSO,” *Prog. Electromagn. Res.* **109** 325–343 (2010).
- [13] M. Saritha, K.P. Joseph, and A.T. Mathew, “Classification of MRI brain images using combined wavelet entropy based spider web plots and probabilistic neural network,” *Pattern Recogn. Lett.* **34**(16) 2151-2156 (2013).
- [14] Y.D. Zhang, Z.C. Dong, G.L. Ji, “Effect of spider-web-plot in MR brain image classification,” *Pattern*

Recogn. Lett. **62**, 14-16 (2015).

- [15] S. Das, M. Chowdhury, M.K. Kundu. "Brain MR Image Classification Using Multiscale Geometric Analysis of Ripplet," Prog. Electromagn. Res. **137**, 1-17 (2013).
- [16] F.J. Gilbert, S.M. Astley, M.G. Gillan, O.F. Agbaje, M.G. Wallis, J. James, C.R. Boggis, S.W. Duffy, "Single Reading with Computer-Aided Detection for Screening Mammography," N. Engl. J. Med. **359**, 1675-1684 (2008).
- [17] P. Taylor, J. Champness, R. Given-Wilson, K. Johnston, H. Potts. "Impact of computer-aided detection prompts on the sensitivity and specificity of screening mammography," Health Technol. Asses. **9** (6), 1-70 (2005).
- [18] J.J. Fenton, S.H. Taplin, P.A. Carney, L. Abraham, E.A. Sickles, C. D'Orsi, *et al.* "Influence of computer-aided detection on performance of screening mammography," N. Engl. J. Med. **356** (14), 1399-409 (2007).
- [19] N. Wu, G. Gamsu, J. Czum, B. Held, R. Thakur, G. Nicola. "Detection of small pulmonary nodules using direct digital radiography and picture archiving and communication systems," J. Thorac. Imaging **21** (1), 27-31 (2006).
- [20] N. Petrick, M. Haider, R.M. Summers, S.C. Yeshwant, L. Brown, E.M. Iuliano, A. Louie, J.R. Choi, P.J. Pickhardt. "CT colonography with computer-aided detection as a second reader: observer performance study," Radiology **246** (1), 148-56 (2008).
- [21] S. Halligan, D.G. Altman, S. Mallett, S.A. Taylor, D. Burling, M. Roddie, L. Honeyfield, J. McQuillan, H. Amin, J. Dehmeshki. "Computed tomographic colonography: assessment of radiologist performance with and without computer-aided detection," Gastroenterology **131** (6): 1690-9 (2006).
- [22] E. Arnoldi, M. Gebregziabher, U. J. Schoepf, R. Goldenberg, L. Ramos-Duran, P. L. Zwerner, K. Nikolaou, M. F. Reiser, P. Costello, C. Thilo. "Automated computer-aided stenosis detection at coronary CT angiography: initial experience," Eur. Radiol. **20** (5), 1160-7 (2010).
- [23] E. J. Halpern, D. J. Halpern. "Diagnosis of coronary stenosis with CT angiography: comparison of automated computer diagnosis with expert readings," Acad. Radiol. **18** (3), 324-33 (2011).
- [24] K.W. Kang, H.J. Chang, H. Shim, Y.J. Kim, B.W. Choi, W.I. Yang, J.Y. Shim, J. Ha, N. Chung, "Feasibility of an automatic computer-assisted algorithm for the detection of significant coronary artery disease in patients presenting with acute chest pain," Eur. J. Radiol. **81** (4), e640-6 (2012).
- [25] A. Padma, and R. Sukanesh, "Segmentation and Classification of Brain CT Images Using Combined Wavelet Statistical Texture Features," Arab. J. Sci. Eng. **39**(2), p. 767-776 (2014).
- [26] Y.D. Zhang, S.H. Wang, Z.C. Dong, "Classification of Alzheimer Disease Based on Structural Magnetic Resonance Imaging by Kernel Support Vector Machine Decision Tree," Prog. Electromagn. Res. **144**, 185-191 (2014).

- [27] Z.C. Dong, "Detection of subjects and brain regions related to Alzheimer's disease using 3D MRI scans based on eigenbrain and machine learning," *Front Comput. Neurosc.* **66** (9), 1–15 (2015).
- [28] H. Arimura, Q. Li, Y. Korogi, T. Hirai, H. Abe, Y. Yamashita, S. Katsuragawa, R. Ikeda, and K. Doi, "Automated computerized scheme for detection of unruptured intracranial aneurysms in three-dimensional magnetic resonance angiography," *Acad. Radiol.* **11**, 1093-1104 (2004).
- [29] H. Arimura, Q. Li, Y. Korogi, T. Hirai, H. Abe, Y. Yamashita, S. Katsuragawa, R. Ikeda, and K. Doi, "Development of CAD scheme for automated detection of intracranial aneurysms in magnetic resonance angiography," in *Proceedings of the 18th International Congress and Exhibition* (International Congress Series, Elsevier, 2004), **1268**, 1015-1020.
- [30] T. Hirai, Y. Korogi, H. Arimura, S. Katsuragawa, M. Kitajima, M. Yamura, Y. Yamashita, and K. Doi, "Intracranial Aneurysms at MR Angiography: Effect of Computer-aided Diagnosis on Radiologists' Detection Performance," *Radiol.* **237**, 605-610 (2005).
- [31] S. Kobashi, K. Kondo, and Y. Hata, "Computer-aided diagnosis of intracranial aneurysms in MRA images with case-based reasoning," *IEICE Trans. Inf. Syst.* **E89**, 340 – 350 (2006).
- [32] S. Kakeda, Y. Korogi, H. Arimura, T. Hirai, S. Kasuragawa, T. Aoki, and K. Doi, "Diagnostic accuracy and reading time to detect intracranial aneurysms on MR angiography using a computer-aided diagnosis system," *Am. J. Roentgenol.* **190**, 459-465 (2008).
- [33] A. Lauric, E. Miller, S. Frisken, and A.M. Malek, "Automated detection of intracranial aneurysms based on parent vessel 3D analysis," *Med. Image Anal.* **14**, 149-159 (2010).
- [34] X. Yang, D.J. Blezek, L.T. Cheng, W.J. Ryan, D.F. Kallmes, and B.J. Erickson, "Computer-aided detection of intracranial aneurysms in MR angiography," *J. Digit. Imaging* **24**, 86-95 (2011).
- [35] I. Larrabide, M. Cruz Villa-Uriol, R. Cárdenes, J.M. Pozo, J. Macho, L. San Roman, J. Blasco, E. Vivas, A. Marzo, D.R. Hose, and A.F. Frangi, "Three-dimensional morphological analysis of intracranial aneurysms: a fully automated method for aneurysm sac isolation and quantification," *Med. Phys.* **38**, 2439-2449 (2011).
- [36] I.L. Šteřán-Buksakowska, J.M. Accurso, F.E. Diehn, J. Huston, T.J. Kaufmann, P.H. Luetmer, C.P. Wood, X. Yang, D.J. Blezek, R. Carter, C. Hagen, D. Hořinekd, A. Hejčld, M. Ročেকে, and B.J. Erickson, "Computer-aided diagnosis improves detection of small intracranial aneurysms on MRA in a clinical setting," *Am. J. Neuroradiol.* **35**, 1897-1902 (2014).
- [37] C.M. Hentschke, O. Beuing, H. Paukisch, C. Scherlach, M. Skalej, and K.D. Tnnies, "A system to detect cerebral aneurysms in multimodality angiographic data sets," *Med. Phys.* **41**, 091904 (11pp.) (2014).
- [38] H. Arimura, Q. Li, Y. Korogi, T. Hirai, H. Abe, Y. Yamashita, S. Katsuragawa, R. Ikeda, and K. Doi, "Computerized detection of intracranial aneurysms for three-dimensional MR angiography: feature

- extraction of small protrusions based on a shape-based difference image technique,” *Med. Phys.* **33**, 394-401 (2006).
- [39] Y. Sato, S. Nakajima, N. Shiraga, H. Atsumi, S. Yoshida, T. Koller, G. Gerig, and R. Kikinis, “Three-dimensional multi-scale line filter for segmentation and visualization of curvilinear structures in medical images,” *Med. Image Anal.* **2.2**, 143-168, (1998).
- [40] A. F. Frangi, W. J. Niessen, K. L. Vincken, and M. A. Viergever, “Multiscale vessel enhancement filtering,” In *Medical Image Computing and Computer-Assisted Intervention—MICCAI’98*. (Springer Berlin Heidelberg, 1998), pp. 130-137.
- [41] A.C. Burleson, C.M. Strother, and V.T. Turitto, “Computer modeling of intracranial saccular and lateral aneurysms for the study of their hemodynamics,” *Neurosurgery* **37**, 774-784 (1995).
- [42] M.A. Bernstein, J. Huston, C. Lin, G.F. Gibbs, and J.P. Felmlee, “High - resolution intracranial and cervical MRA at 3.0 T: Technical considerations and initial experience,” *Magnet. Reson. Med.* **46**, 955-962 (2001).
- [43] T.J. Kaufmann, J. Huston, and H.J. Cloft. “A prospective trial of 3T and 1.5 T time-of-flight and contrast-enhanced MR angiography in the follow-up of coiled intracranial aneurysms,” *Am. J. Neuroradiol.* **31**, 912-918 (2010).
- [44] Y. Sato, C. Westin, A. Bhalerao, S. Nakajima, N. Shiraga, S. Tamura, and R. Kikinis, “Tissue classification based on 3D local intensity structures for volume rendering,” *IEEE Trans. Vis. Comput. Graph.* **6**, 160-180 (2000).
- [45] T. Lindeberg, “Scale Selection Properties of Generalized Scale-Space Interest Point Detectors,” *J. Math. Imaging. Vis.* **46**(2) , 177-210 (2013).
- [46] T. Lindeberg, “Image Matching Using Generalized Scale-Space Interest Points”, Springer Berlin Heidelberg, pp 355-367 (2013).
- [47] T. Lindeberg, “Image matching using generalized scale-space interest points,” *J. Math. Imaging. Vis.* **52**(1), 3-36 (2015).
- [48] Y. Shinohara, T. Yoshimoto, Y. Fukuuchi, and S. Ishigami, “The Joint Committee on Guidelines for the Management of Stroke,” in *Japanese Guidelines for the Management of Stroke* (in Japanese). (Tokyo, Kyowa Kikaku 2004), pp. 1–234.
- [49] Z. Jin, H. Arimura, Y. Korogi, F. Yamashita, and M. Sasaki, “Evaluation of an Automated Identification System of Unruptured Intracranial Aneurysm Candidates Based on a Blob Structure Enhancement Filter at 3.0 T Magnetic Resonance Angiography,” *IEICE Technical Report* **113**, 249-253 (2014).
- [50] M. Dundar, G. Fung, L. Bogoni, M. Macari, A. Megibow, and B. Rao, “A methodology for training and validating a CAD system and potential pitfalls,” in *Proceedings of the 18th International Congress and Exhibition* (International Congress Series, Elsevier, 2004), **1268**, 1010-1014.

- ^[51] D.P. Chakraborty and L.H. Winter, “Free-response methodology: alternate analysis and a new observer-performance experiment,” *Radiol.* **174**, 873-881 (1990).
- ^[52] I. Uwano, K. Kohsuke, Y. Fumio, J. Goodwin, S. Higuchi, K. Ito, T. Harada, A. Ogawa, and M. Sasaki, “Intensity inhomogeneity correction for magnetic resonance imaging of human brain at 7T,” *Med. Phys.* **41**, 022302 (9pp.) (2014).

Achievements

Journal papers

1. Jin Z., Arimura H., Kakeda S., Yamashita F., Sasaki M., and Korogi Y. An ellipsoid convex enhancement filter for detection of asymptomatic intracranial aneurysm candidates in CAD frameworks. *Medical physics*, 43(2), 951-960, 2016.
2. Jin Z., Arimura H, Shioyama Y, et al. Computer-Assisted Delineation of Lung Tumor Regions in Treatment Planning CT Images with PET/CT Image Sets Based on an Optimum Contour Selection Method. *Journal of Radiation Research*. 55(6), 1153-62, 2014

Non-refereed Publications

1. Jin Z., Arimura H, Kakeda S, et al, A novel ellipsoid convex enhancement filter for boosting the performance in detection of asymptomatic intracranial aneurysms at 3.0 T magnetic resonance angiography IEICE Technical Report,, vol. 115, no. 401, MI2015-126, pp. 257-261, 2016.
2. Jin Z., Arimura H, Sasaki M, et al. Evaluation of an Automated Identification System of Unruptured Intracranial Aneurysm Candidates Based on a Blob Structure Enhancement filter at 3.0 T Magnetic Resonance Angiography. IEICE Technical Report, Vol.113, 249-253, 2014.
3. Jin Z., Arimura H, Shioyama Y, et al. Computer-aided Delineation of Lung Tumor Regions in Treatment Planning CT Images and PET/CT Images Using Localized Level Set Approach. IEICE Technical Report, Vol.112, 49-51, 2013.
4. Jin Z., Arimura H, Shioyama Y et al. Automated Contouring of Tumor Regions in Treatment Planning CT Images Using PET/CT Images Based on a Localized Level Set Method. *Japanese Journal of Medical Physics*, Vol.32 sup 3, 133-134, 2012.

International conferences presentations

1. Jin Z., Arimura H, Kakeda S, et al. Impact of a novel enhancement filter for various ellipsoid convex shapes on CAD frameworks of asymptomatic unruptured intracranial aneurysms. The 13th South-East Asia Congress of Medical Physics, Yogyakarta, Indonesia, December 2015.

2. Jin Z, Arimura H, Korogi Y, et al. Impact of inhomogeneity correction on a computer-aided diagnostic framework for asymptomatic unruptured intracranial aneurysms using magnetic resonance angiography. International Forum on Medical Imaging in Asia, Tainan, Taiwan, January 2015.
3. Jin Z, Arimura H, Shioyama Y, Sasaki M, et al. Computer-aided Delineation of Tumor Regions for Lung Cancer in Multimodality Images by Localized Level Set Method. 17th International Conference on the Use of Computers in Radiation Therapy in Melbourne, Australia, May 2013.
4. Jin Z, Arimura H, Shioyama Y, Toyofuku F, et al. Computer-aided radiotherapy: extraction of bronchial regions in treatment planning CT images World Congress on Medical Physics and Biomedical Engineering in Beijing, China, May 2012.

Conference presentations in Japan

1. Jin Z, Arimura H, Kakeda S, et al. 3.0 T MRA 画像における未破裂脳動脈瘤支援診断に対する選択的凸領域強調フィルタ. 第 43 回日本磁気共鳴医学会大会, Tokyo, September 2015.
2. Jin Z, Arimura H, Kakeda S, et al. A Novel Ellipsoid Convex Enhancement Filter for Boosting the Performance in Detection of Asymptomatic Intracranial Aneurysms at 3.0 T Magnetic Resonance Angiography. IEICE, Okinawa, January 2016.
3. Jin Z, Arimura H, Sasaki M, et al. Evaluation of an Automated Identification System of Unruptured Intracranial Aneurysm Candidates Based on a Blob Structure Enhancement filter at 3.0 T Magnetic Resonance Angiography. IEICE, Okinawa, January 2014.
4. Jin Z, Arimura H, Shioyama Y, et al. Computer-aided Delineation of Lung Tumor Regions in Treatment Planning CT Images and PET/CT Images Using Localized Level Set Approach. IEICE, Okinawa, January 2013.
5. Jin Z, Arimura H, Kuwazuru J, Shioyama Y, Magome T, Nakamura K, Honda H, Toyofuku F, Sasaki, M Hirata H., Automated Contouring of Tumor Regions in Treatment Planning CT Images Using PET/CT Images Based on a Localized Level Set Method (p133-134), 第 104 回医学物理学学会 JSMP(つくば), 2012.09.15.

6. Jin Ze, Arimura H, Shioyama Y, Fukuta M, Magome T, Kakiuchi G, Nakamura K, Honda H, Hirata H, Toyofuku F., Development of an automated method for segmentation of bronchial regions in planning CT images (p.237), 第 103 回日本医学物理学会学術大会(横浜), 2012.04.14.

Award:

English Presentation Award at the 105th Scientific Meeting of the Japan Society of Medical Physics (JSMP), Apr.14, 2013

Foundation:

1. キン タク, 「統計的生物数理モデルを用いた脳動脈瘤ロバスト検出システム」
研究課題番号：15J03586 日本学術振興会 DC2, 特別研究員奨励費 日本学術振興会 特別研究員奨励費 1700 千円, 2015 年度～2016 年度. (保健学科指導教員：有村秀孝)

Fellowship and Scholarship:

2012 – 2013 Japanese Government (Monbukagakusho) Scholarships

2014 – 2015 Recipient of Otsuka Toshimi Scholarship Foundation

2015 – Present Research Fellow of the Japan Society for the Promotion of Science